Timing Evaluation of Iridium Satellite Time and Location Signal: Measurement-Level Implementation and Receiver Hardware Time Interval Comparison

by

Austin M. Smith

A thesis submitted to the Graduate Faculty of
Auburn University
in partial fulfillment of the
requirements for the Degree of
Master of Science

Auburn, Alabama
December 9, 2023

Approved by

David M. Bevly, Chair, Bill and Lana McNair Distinguished Professor of Mechanical Engineering
Scott M. Martin, Assistant Professor of Mechanical Engineering
Chad G. Rose, Assistant Professor of Mechanical Engineering

Abstract

This thesis assesses the accuracy, stability, and convergence rates of receiver timing solutions with the Iridium Satellite Time and Location (STL) signal through two studies. In the first experiment, an Extended Kalman Filter (EKF) and a Weighted Least Squares (WLS) solution are used to estimate the clock states of a static receiver at an antenna location which is known and unknown, respectively. In the second experiment, a 1-PPS (Pulse-Per-Second) time interval study is conducted with two, commercially-available Jackson Labs Technologies STL-2600 receivers, which are both provided a precise position. Both tests are conducted using an on-board Temperature Compensated Crystal Oscillator (TCXO) and external rubidium oscillator.

Nanosecond-level timing solutions from Global Navigation Satellite Systems (GNSS), such as the Global Positioning System (GPS), are integrated into many personal and industrial systems, including transportation, communications systems, electrical power grids, and financial institutions. However, due the orbital altitude of the satellites, the received signal power of the end user is critically low, resulting in vulnerable timing solutions. The Low-Earth Orbit (LEO) Iridium constellation orbits significantly closer to Earth's surface, ensuring higher received signal strength. While the system was originally intended for communications, the satellites have been updated to broadcast the STL message, which can be used for navigation applications.

The results of these experiments indicate that the Iridium STL signal is capable of providing GNSS-independent, nanosecond-level timing accuracy for stationary receivers. Throughout the 120 hours of data collected, the receiver timing accuracy was maintained to within a mean timing error of less than 205 nanoseconds. The timing state estimation experiment demonstrates a substantial improvement in timing performance when the receiver position is provided to the estimator, resulting in standard deviations of less than 1 nanosecond per second. The 1-PPS time interval experiment shows the off-the-shelf capabilities of the STL receiver to be accurate to within 110 nanoseconds of deviation and approximately 500 nanoseconds of error at all times. The second experiment also indicates the maximum timing error and deviation can be reduced when a high-fidelity, rubidium oscillator is integrated into the receiver hardware.

Acknowledgments

I would first like to thank the Lord for providing me with the opportunity to continue my education through graduate school. It is by His blessings that any of this work is possible. I would also like to thank my fiancé Katie, parents, brother, and sister for their overwhelming support and encouragement through the good and bad times. I owe Dr. David Bevly a debt of gratitude for offering me a graduate research position with the GPS and Vehicle Dynamics Laboratory (GAVLAB). Dr. Bevly made sure to be available for direction, discussion, and pick-up basketball. As both an advisor and professor, his wisdom has guided my work and made me a better engineer. As for colleagues, I would like to thank the entire GAVLAB for their willingness to help with coursework or research. Graduate school has been very challenging and, at times, exhausting, but the experiences and fellowship far outweigh the struggles. To everyone mentioned and unmentioned, thank you.

”The Lord makes firm the steps of the one who delights in Him; though he may stumble, he will not fall, for the Lord upholds him with His hand.” - Psalm 37:23-24

Table of Contents

List of Figures

List of Tables

Chapter 1

Introduction

1.1 Motivation

Since the Global Positioning System (GPS) became fully-operational in 1993, Position, Navigation, and Timing (PNT) solutions from Global Navigation Satellite Systems (GNSS) have been integrated into an increasing number of government, industrial, and personal systems, such as transportation, agriculture, communications services, electrical power grids, and financial institutions [1, 2]. However, low received signal strength and environmental conditions, including urban canyons, indoor applications, and electronic radio interference, compromise the integrity of the navigation solutions [3–5]. While satellite-based PNT solutions have aided and enabled technological advances, the functionality of these systems has become increasingly dependent on accurate navigation and timing information. Among the potential consequences of a GNSS outage are: a threat to public safety, loss of services, and an estimated financial cost of \$1 billion per day [6]. Therefore, PNT services to backup or complement GPS and other GNSS are critical.

For two primary reasons, the PNT capabilities of existing Low-Earth Orbit (LEO) satellite constellations have generated interest in recent years. First, LEO satellites orbit significantly closer to Earth's surface, resulting in higher received signal power and more resilient solutions [7]. Second, also due to lower orbital altitude, Line-Of-Sight (LOS) vectors from LEO satellites change significantly faster, reducing multipath errors and improving Doppler positioning performance [8]. One of the primary drawbacks to LEO navigation is the lack of satellite Position, Velocity, and Timing (PVT) information available from the downlink transmission, which is required for receiver state estimation. Therefore, in many implementations of LEO-based navigation, either additional information must be known at the user-level, or the satellite states must be estimated in the navigation filter.

The Iridium constellation is a promising LEO candidate as a backup or complement to the PNT services of GNSS. The constellation provides full coverage of the Earth's surface, ensuring that at least one satellite will be in view at any time [9]. Also, the Iridium satellites broadcast a downlink transmission containing the Satellite Time and Location, or STL, message. The STL signal can be demodulated and decoded to extract measurements of the satellite PVT states, which can be used in navigation frameworks similar to traditional GNSS. The objective of this thesis is to assess the accuracy, stability, and convergence rates of receiver timing solutions with the Iridium STL signal.

1.2 Background and Literature Review

> *"For what is time? Who can easily and briefly explain it? Who can even comprehend it in thought or put the answer into words? Yet is it not true that in conversation we refer to nothing more familiarly or knowingly than time? And surely we understand it when we speak of it; we understand it also when we hear another speak of it. What, then, is time? If no one asks me, I know what it is. If I wish to explain it to him who asks me, I do not know."*
>
> - St. Augustine[1]

1.2.1 Timing Overview

The concept of time is a complex topic, with varying definitions amongst academics and scholars. In the realm of science and engineering, time is often represented as an elapsed period between two events. In other words, *relative* time is generally desirable when describing how systems behave and interact. A simple example of relative timing can be found in the rudimentary physics problem of a free-falling object. If one wishes to determine the object's time-of-flight, the release-time can be set as zero, and the time of impact can be calculated.

---

[1] From *Augustine: Confessions*, translated by Albert C. Outler

This time is observed *relative* to the initial system conditions, as opposed to *absolutely* in the spacetime manifold. For the concepts presented in this thesis, three primary relative timing metrics are used for hardware configurations and results comparison.

The first timing metric used is GPS time, which defines the current time relative to 0:00 Coordinated Universal Time (UTC) on January 6, 1980. GPS time is continuously measured in GPS weeks and seconds, and does not account for leap seconds, resulting in a changing offset relative to UTC [10]. After accounting for this offset, GPS time error relative to UTC is estimated to be less than 30 nanoseconds, 95% of the time [11], rendering these timing messages useful for many applications, such as synchronizing control systems, timestamping financial transactions, and remote sensor synchronization [12, 13]. Figure 1.1 describes an example network of three systems utilizing GNSS satellites for timing synchronization. In the example, System 1, 2, and 3 are disciplined to the same time scale, without the need for wired connections or local atomic oscillators to maintain precise timing. Although not discussed in this thesis, it should be noted that other GNSS constellations do not utilize the GPS timescale. For example, Russia's Global'naya Navigatsionnaya Sputnikovaya Sistema, or *GLONASS*, abides by GLONASS time, which includes leap seconds to remain on the UTC timescale [14]. Further details regarding timing estimation are described in Chapter 3.

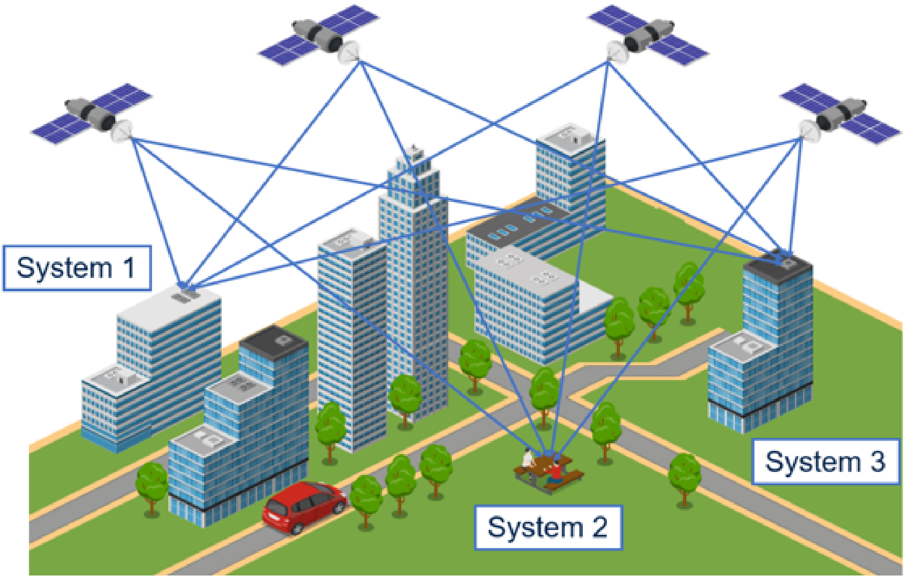

Figure 1.1: Example Remote Network Timing Synchronization

The second two timing metrics used in this thesis are a 1 Hz, or 1-Pulse-Per-Second (1-PPS), and a 10 MHz reference signal. Both of these signals are voltage outputs from oscillators incorporated into navigation hardware configurations. When locked to GPS, most receiver clocks are steered to maintain accurate time. GNSS-disciplined timing reference signals can be applied to a variety of applications, including wireless sensor communication and synchronization, electrical power grids, and telecommunication systems [15–17]. The usage of the 1-PPS and 10 MHz timing reference signals for this work is presented briefly in Chapter 3 and in-depth in Chapter 4.

1.2.2 Opportunistic Navigation

While perhaps not intuitive, timing is a crucial dimension incorporated into navigation solutions, which is discussed in Chapter 2. Although GNSS is currently the gold standard for satellite-based PNT services, the vulnerabilities discussed in Section 2.3.2 emphasize the need for a backup or complement system. One of the primary difficulties in satisfying necessary timing requirements is many of the candidate systems were not originally designed for navigation purposes or available for public use. The usage of alternative signals to GNSS falls into one of two categories: opportunistic and permissive. The fundamental difference between the two is opportunistic frameworks exploit existing signals for navigation purposes, without requiring any data from the signal, while permissive frameworks are capable of demodulating the signal and extracting a data message.

In the realm of opportunistic navigation, signals of opportunity (SOPs) is a term defining ambient signals that can be acquired and tracked for navigation applications. SOP emitters can be located either on the Earth's surface or in orbit. Examples of terrestrial-based emitters are audio, Wi-Fi, television, and cellular signals [18–20]. While land-based SOPs can be used for navigation applications in a specific geographic area, they are only effective within the range or visibility of the emitter. For this reason, space-based systems prove to be more useful for global PVT estimation.

For reasons discussed later in Section 2.4, LEO satellite constellations have gathered the most interest as a satellite-based backup or complement to GNSS services. The Globalstar, Iridium, Orbcomm, and Starlink constellations are examples of potential LEO-based SOP sources [21–23]. While ambient signals are widely available for acquisition, knowledge of the transmitting Satellite Vehicle (SV) states, such as satellite PVT, cannot be extracted from the signal in opportunistic frameworks. A popular technique used to gather the necessary information to form a navigation solution is extracting a Doppler shift measurement from SOPs and calculating a SV position and velocity derived from a Two-Line Element set (TLE) [22, 24, 25]. However, with this method, the accuracy of the receiver PVT solution is limited due to orbital perturbations causing satellite position errors ranging from 100 meters to several kilometers [26]. Other approaches to obtaining satellite PVT states include the Simultaneous Tracking And Navigation (STAN) [27, 28] and differential Doppler navigation [29, 30] frameworks.

While opportunistic techniques are capable of providing receiver position and velocity state estimates, on-board satellite timing information is necessary to estimate and maintain receiver clock accuracy, particularly for extended time periods. Therefore, for timing applications, the permissive usage of LEO satellite signals is required for timing applications. As is shown in Section 2.4.2, the Iridium Satellite Time and Location (STL) system is currently the primary candidate for commercial, LEO-based timing solutions.

1.2.3 Timing Evaluation with Iridium STL

In January 2016, researchers conducted a timing study of an SiRFstarVxp STL EVK-1 receiver equipped with a standard, on-board Temperature Compensated Crystal Oscillator (TCXO) [31]. The test demonstrated the receiver indoor timing capabilities and deep-indoor signal penetration. During the 24-hour indoor timing test, the receiver maintained sub-microsecond-level timing accuracy. The 9.5-hour signal penetration test only measured detected STL bursts. For the majority of the test, the time between detected bursts was under 5 seconds, compared to an approximately 1 second in outdoor environments. The time between received burst exceeded 2 minutes four times throughout the test period.

A January 2018 study assessed the timing capabilities of a Satelles STL EVK-2 receiver [32]. The test consisted of three receiver hardware configurations. Configuration 1 used a highly-stable rubidium receiver clock input and assumed a precisely-known, static antenna position. Configuration 2 consisted of the same hardware configuration as Configuration 1, but assumed a static, unknown receiver position. Configuration 3 utilized a local STL reference station, which used a GPS-derived timebase, to transmit error measurements to the user equipment. The results of the study were generated by comparing the 1-PPS output of the EVK-2 receiver with a GNSS reference. With an outdoor antenna, Configuration 1 required 6 hours to converge to the desired accuracy level and performed with a mean error of -11 nanoseconds, standard deviation of 30 nanoseconds, and maximum error of 170 nanoseconds over the 14-day period. Configuration 2 was initialized within 5 kilometers of the true location, and performed with a mean error of -141 nanoseconds, standard deviation of 107 nanoseconds, and pre- and post-convergence error of 656 and 420 nanoseconds, respectively.

Timing capabilities of the Satelles STL EVK-2 receiver were also demonstrated in a January 2021 Department of Transportation study [33]. One of the tests conducted was a 72-hour 1-PPS time interval comparison. In this study, two receivers were equipped with a rubidium and Oven Controlled Crystal Oscillator (OCXO). The rubidium-disciplined receiver configuration performed with a median error of 25 nanoseconds, standard deviation of 31 nanoseconds, and maximum error of 92 nanoseconds, and the OXCO-disciplined receiver performed with a median error of 34.25 nanoseconds, standard deviation of 41 nanoseconds, and maximum error of 209 nanoseconds.

Most recently, a January 2023 study conducted by Satelles, Inc. and the National Institute of Standards & Technology assessed the 1-PPS accuracy of a Satelles STL EVK-2 receiver with both an OXCO and a rubidium oscillator [34]. This study took extensive measures to calibrate the receivers, which included multiple calibration periods of either 24 or 48 hours. Over a 30-day period, the calibrated, OCXO-disciplined receiver performed with an average time offset of 18 nanoseconds and a peak-to-peak variation of less than 80 nanoseconds, while the rubidium-disciplined receiver performed with a similar average offset and a peak-to-peak variation of 300 nanoseconds.

From the literature presented, several common themes can be identified. First, statistical parameters of the 1-PPS timing capabilities are the primary metric used to quantify the performance of the receiver, as it is a direct output of both the STL user equipment and GNSS timing reference systems. Therefore, only a time interval measuring device is necessary to calculate a time delay measurement between the rising edge of the 1-PPS square waves. Second, a primary interest in several of the studies is the effects of including a high-fidelity, external oscillator into the STL receiver hardware configuration. Finally, knowledge of the antenna location reduces the degrees of freedom of the timing solution and augments the measurement model within the receiver. Therefore, theoretically, knowledge of the receiver position improves the fidelity of the timing solution.

1.3 Contributions

The work presented in this thesis aims to perform similar experiments to those published in the prior art with a newly-released, commercially-available STL receiver module, as well as compare additional timing metrics and hardware configurations. From the literature, the receiver 1-PPS output used is the primary metric to assess the performance of the STL hardware. However, many timing applications utilize GPS time for timestamping, which requires an estimate from the navigation filter, as opposed to an output signal from the receiver module. In this thesis, timing estimation frameworks for a static antenna at a known and unknown location are presented, and clock bias and drift estimates are used to quantify and compare the timing performance. Additionally, in the case of a known receiver position, analysis of the fidelity of the position solution is conducted.

Much of the work presented in this thesis is built upon a paper titled, ”Precision Timing with LEO Satellite Time and Location Signals” [35]. A more in-depth description of the processes, additional results, and further analysis are provided in this thesis. The primary interests of this work are to implement and compare multiple measurement-level timing state estimation algorithms under various receiver scenarios, evaluate the performance of Iridium STL receiver hardware, and assess the effect of receiver input clock on timing accuracy. The contributions of this thesis are:

- Implement and test application-specific timing estimation algorithms under various static receiver conditions
- Assess and compare accuracy, stability, and convergence rates of timing state estimates
- Identify error sources, such as satellite visibility and geometry
- Compare 1-PPS timing accuracy of a newly-released, commercially-available receiver with varying hardware and firmware configurations

1.4 Thesis Outline

This thesis consists of 5 chapters. This chapter has introduced the motivation for the work and emphasizes the importance and use cases of satellite-based timing solutions. This chapter also introduced LEO satellite constellations as a potential backup or complement to GNSS and described the difference between opportunistic and permissive usage of these systems. The Iridium STL service has been identified as the primary, satellite-based timing source for this thesis, in which timing estimation frameworks and receiver time interval outputs are tested. Lastly, a concise representation of the contributions of this thesis is presented.

Chapter 2 provides an overview of satellite navigation, beginning with the history and development of GNSS. The specifics of the GPS system are discussed, including coordinate frames, signal properties, position and time estimation algorithms, and vulnerabilities. Chapter 2 then transitions into the Iridium constellation and STL system and discusses the similarities and differences to GPS. The advantages and disadvantages of STL-based navigation and timing are presented.

Chapter 3 introduces the first study conducted for this thesis. First, the correlation between navigation clock states and timing is presented. Next, an overview of the receiver, clocks, and data collection hardware used is presented. For estimation, a timing-state Extended Kalman Filter and a Weighted Least Squares solution using pseudorange and Doppler shift measurement models are derived and implemented. Finally, results of the timing states, estimate covariance, convergence, analysis, and conclusions are discussed, and receiver scenarios and hardware configurations are discussed.

Chapter 4 consists of the second experiment contained in this thesis. Additional hardware and firmware settings are described, and the 1-PPS time interval experiment is presented. Data collection configurations and parameters are described. The results are presented as raw output data from the time interval measurement device, along with a statistical analysis and comparison between the configurations.

Chapter 5 provides conclusions obtained from the two experiments conducted for this thesis by first summarizing its contents. Findings regarding the usage of Iridium STL as a complement or backup to the timing capabilities of GNSS are discussed. Finally, closing remarks and potential avenues of future exploration in the field are presented.

Chapter 2

Overview of Satellite Navigation

2.1 History of GPS

The term GNSS denotes several satellite systems that provide navigation information to user receiver equipment for positioning and timing applications. Examples of currently operational GNSS constellations are the United States' GPS, Russia's GLONASS, China's Bei-Dou, Japan's QZSS, and the European Union's GALILEO. For the purposes of this thesis, GPS is considered as the primary GNSS constellation, as it is the original and most widely-used navigation satellite network.

Prior to the conception of satellite navigation, on October 4, 1957, Sputnik 1 was launched, which is pictured in Figure 2.1. From signals transmitted by the satellite, scientists at John Hopkins University observed large Doppler shifts, which were used to determine the satellite orbit with a single ground tracking station. The scientists promptly thought to reverse the process by using the Doppler shift measurement from a satellite with a known orbit to calculate the position of a receiver on Earth's surface. The United States Department of Defense funded the project under the title *TRANSIT*, which began in 1959. TRANSIT was declared operational for official and civilian use in January 1964 and July 1967, respectively. The network consisted of LEO satellites orbiting at an altitude of 1,000 kilometers, and signals were transmitted at two frequencies, 149.00 and 399.97 MHz. Although the project was discontinued in December 1996, TRANSIT demonstrated that spacecrafts could be designed to be reliable, and significant advances in satellite orbit prediction algorithms were accomplished [36].

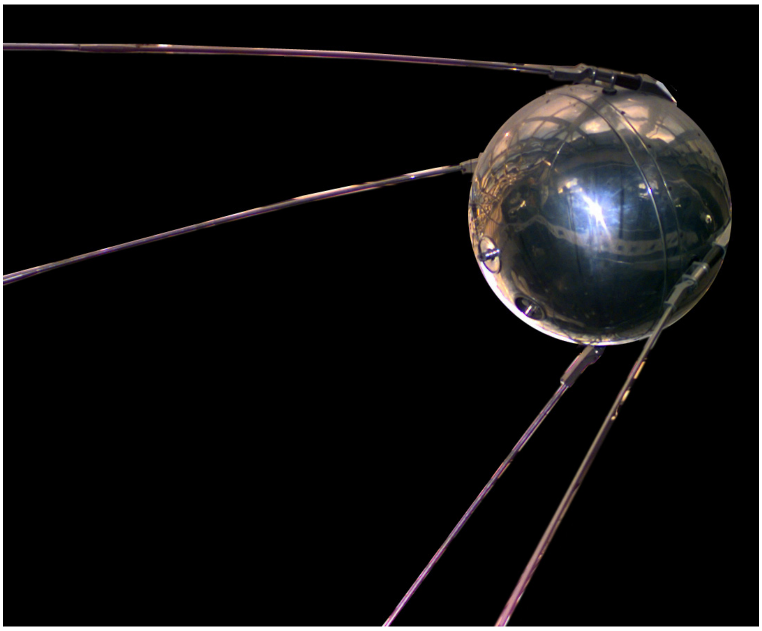

Figure 2.1: Sputnik 1 Satellite [37]

Following the success of TRANSIT, the U.S. Navy and Air Force were interested in further exploring the capabilities of satellite-based navigation and timing. The two efforts were eventually combined under the title *NAVSTAR, the Global Positioning System*, otherwise known as *GPS*. While inspiration from TRANSIT is apparent in GPS, the new system incorporated advanced technologies, mainly clocks and ranging, to improve robustness and performance. The basic architecture was approved by the Department of Defense in 1973, and GPS was declared operational in 1995 [38].

Since development, the GPS network has been refined and modernized to service the needs of users. Amongst the improvements are additional signals, including L2C, L5, and L1C, advanced satellite clocks, and longer spacecraft lifespans. Currently, the GPS constellation is maintained by the U.S. Space Force. The space segment consists of 24 satellites in Medium-Earth Orbit (MEO), and each satellite orbits the Earth twice per day. While only 24 satellites are operational, the Space Force normally flies additional spacecrafts, which can be used as a backup to the existing system [39].

2.2 Fundamentals of Navigation

It has been well-established that the primary function of GPS is to provide users with accurate position, navigation, and timing solutions for static and dynamic platforms. In order to derive these solutions, a basic understanding of the underlying principles is necessary. Amongst these principles are coordinate frames, measurements, and estimation algorithms. In this section, these topics are discussed.

2.2.1 Coordinate Frames

When utilizing GPS position and velocity, it is important to differentiate the coordinate frame of the solution. Navigation states, such as position and velocity, can be estimated either *absolutely* or *relatively*. Absolute positions are defined with respect to the Earth, and their coordinates denote a specific location in a fixed frame. Two of the primary absolute coordinate systems are Earth-Centered, Earth-Fixed (ECEF) and Latitude, Longitude, Altitude (LLA) frames.

The ECEF coordinate system is a Three-Dimensional (3-D), Cartesian frame with its origin at the center of the Earth. Each of the three axes are orthogonal to one another, consisting of an *x*-axis intersecting the prime meridian and the equator, the *y*-axis offset 90° from the prime meridian and intercepting the equator, and the *z*-axis offset 90° from the *x*-*y* plane and running through the Earth's axis of rotation. ECEF coordinates are denoted in the vector form: $[x,\ y,\ z]^T$, in which each value is provided in linear units of meters or kilometers. The ECEF coordinate frame is illustrated in Figure 2.2.

The LLA frame is a geodetic frame and models the Earth as a sphere. The coordinates are defined by two angles, latitude and longitude, and a linear component, altitude. Generally, the angular components are in units of degrees, and the linear component in meters or kilometers. In this frame, the latitude component runs in the east-west direction, with zero being the equator, the longitude angle moves in the north-south direction, with zero running through the prime meridian, and the altitude value is given as a height relative to an Earth model, such as

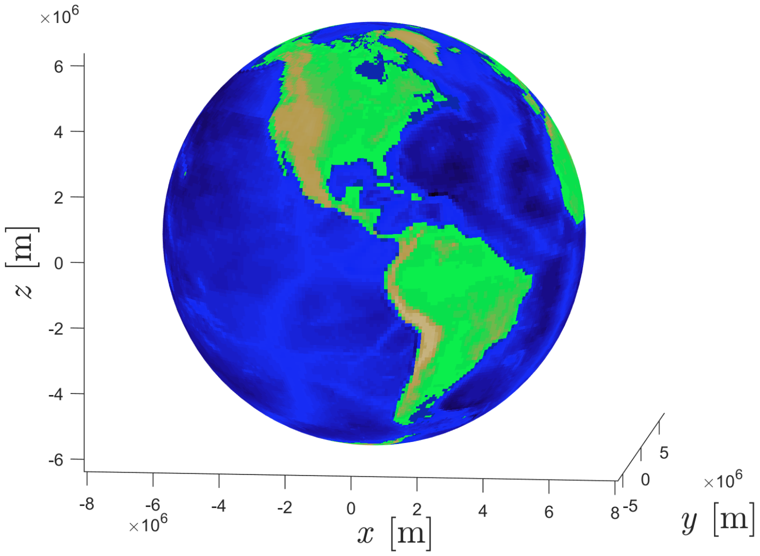

Figure 2.2: ECEF Coordinate Frame Example

Mean Sea Level (MSL) or the WGS84 ellipsoid. An example of the LLA coordinate system is shown in Figure 2.3.

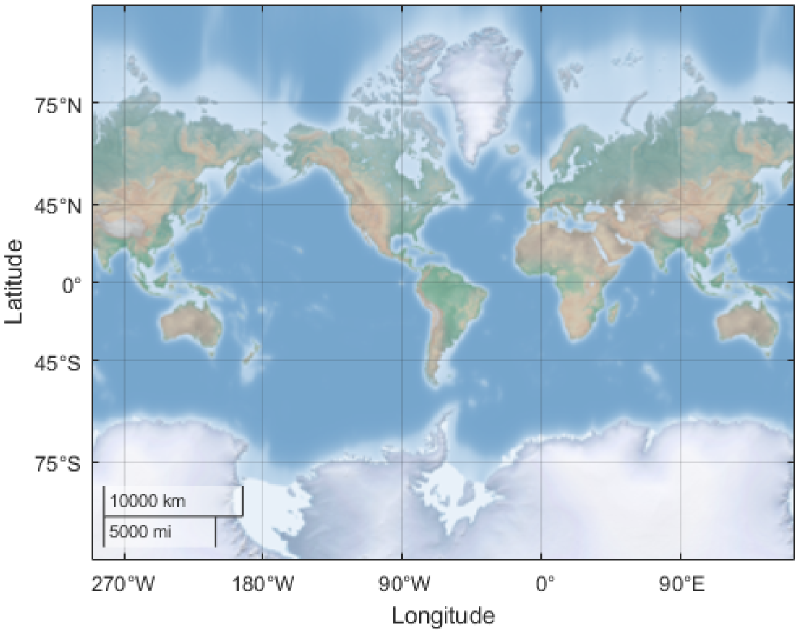

Figure 2.3: LLA Coordinate Frame Example

Instead of defining a receiver's position relative to the Earth as a whole, relative coordinate frames orient position with the origin set to an arbitrary fixed point. In this case, position states are ambiguous, and the ECEF position of the origin must be known in order to obtain a global solution. Examples of relative coordinate systems are North, East, Down (NED) and

East, North, Up (ENU). These frames are useful for describing dynamic scenarios within a set geographic region. However, satellite position and velocity measurements are broadcast in absolute frames, rendering the ECEF and LLA frames more attractive for satellite navigation solutions.

2.2.2 Pseudorange, Pseudorange Rate, and Navigation Measurements

In order to understand how GPS position is calculated, knowledge of the navigation information transmitted from the satellite network is necessary. In this section, it will be apparent that precise timing in both the space segment and user segment is imperative for satellite navigation to function accurately. Additionally, Chapter 3 discusses how these measurements can be used to form timing solutions, whether or not the position of the receiver is known. The primary measurements used in GPS navigation are pseudorange and pseudorange rate. In this thesis, the *tilde* ($\tilde{x}$) notation is used to define the measurement calculation, and *hat* ($\hat{x}$) notation signifies the measurement model.

Pseudorange (ρ) is defined as the measured range between the transmitting satellite and user receiver, which is described in Figure 2.4. In the example, as the satellite moves across the sky, the pseudorange reflects the geometric changes of the LOS vector between the satellite and receiver at each update interval in time (t). The measurement is determined with a Time-of-Arrival (TOA) method, and is primarily used to estimate receiver position. The measurement calculation can be written as:

$$\tilde{\rho} = c(t_{RCVR} - t_{SV}), \tag{2.1}$$

where c is the speed of light, t_{RCVR} is the received time, and t_{SV} is the transmit time from the satellite.

The pseudorange measurement is determined under the assumption that the signal travels at the speed of light. If the Time-Of-Flight (TOF) can be measured, the range between transmitter and receiver can be calculated. However, due to the speed of the signal, small timekeeping inaccuracies in the satellite or receiver clock yield large errors in ranging. For example, a 10-nanosecond clock offset results in a 3-meter range measurement error, and a 50-nanosecond

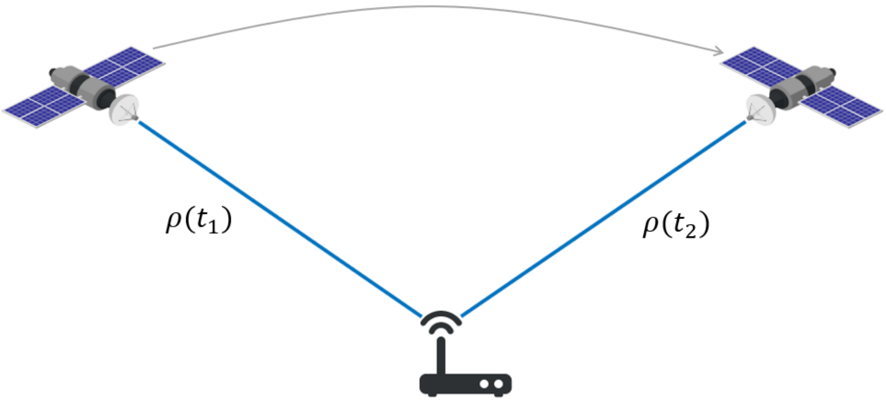

Figure 2.4: Pseudorange Measurement Example

offset yields 15 meters of error. GPS satellites are equipped with highly-stable oscillators, and timing corrections are sent from the system's ground segment to mitigate errors in the satellite clocks. However, most receiver configurations use lower-fidelity oscillators, in which timing errors grow unbounded, if not corrected. For these reasons, the clock offset in the receiver must be incorporated in the measurement model, but satellite timing error may be neglected. The pseudorange measurement can be modelled with four components: geometric range (r), receiver clock bias (b), environmental effects (i.e. ionosphere (I), troposphere (T), multipath (M)), and thermal noise (ε_ρ). The geometric range can be calculated as:

$$r = ||\mathbf{p}_{SV} - \mathbf{p}_{RCVR}|| = \sqrt{(x_{SV} - x_{RCVR})^2 + (y_{SV} - y_{RCVR})^2 + (z_{SV} - z_{RCVR})^2}, \quad (2.2)$$

where $\mathbf{p}_{SV} = [x_{SV},\ y_{SV},\ z_{SV}]^T$ and $\mathbf{p}_{RCVR} = [x_{RCVR},\ y_{RCVR},\ z_{RCVR}]^T$ are the ECEF coordinates of the satellite and receiver, respectively, and the pseudorange measurement model is shown in Equation (2.3).

$$\hat{\rho} = r + cb + I + T + M + \varepsilon_\rho \quad (2.3)$$

Another primary measurement for navigation applications is pseudorange rate ($\dot{\rho}$). Similar to pseudorange, pseudorange rate is not directly measured, but it can be derived from timing. However, instead of measuring the time difference between the transmit and received signal, the pseudorange rate is calculated by detecting the frequency shift between the transmitted and received signal. This change in frequency is called a Doppler shift (f_d), and is caused by the relative motion between the satellite and receiver. A basic example of Doppler shift is shown in Figure 2.5.

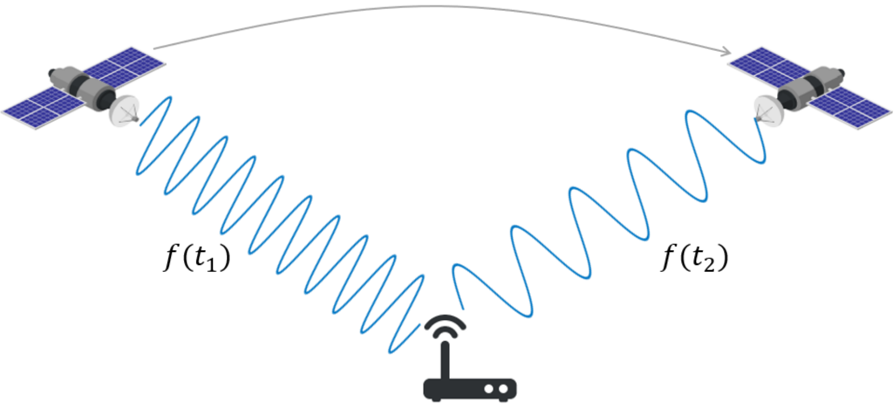

Figure 2.5: Doppler Shift Measurement Example

In Figure 2.5, as a satellite enters the field of view, the distance between the transmit and received antenna is decreasing, and the relative velocity causes the received signal frequency to be higher than the transmitted center frequency. Similarly, as the satellite exits view, the satellite moving away from the receiver results in a received signal that is of lower frequency than the transmitted signal. Doppler shift is defined as the the difference between the transmitted and received signal, which can be expressed as:

$$f_d = f_c - f_r, \tag{2.4}$$

where f_c and f_r are the center and received frequencies, respectively.

With a direct measurement of Doppler shift, the pseudorange rate can be calculated with the wavelength (λ) or center frequency of the signal, which is shown in Equation (2.5).

$$\tilde{\dot{\rho}} = \lambda f_d = \frac{c}{f_c} f_d \tag{2.5}$$

The pseudorange rate measurement can be estimated as the time derivative of Equation (2.3). Considering the pseudorange is modelled as a function of the relative distance between the transmit and received antenna, receiver clock bias, atmospheric effects, and additive noise, the rate can be expressed with the relative velocity, the time derivative of the receiver clock bias and atmospheric effects, and additive noise, which is shown in Equation (2.6).

$$\dot{\hat{\rho}} = \frac{d}{dt}(\hat{\rho}) = \dot{r} + c\dot{b} + \dot{I} + \dot{T} + \varepsilon_{\dot{\rho}} \tag{2.6}$$

Similarly to how the satellite time can be considered perfect for the model of the pseudorange, the drift of the satellite time can be considered to be perfect for the pseudorange rate. However, as receivers are not generally equipped with high-fidelity, atomic oscillators, the change of the receiver bias, or *clock drift* ($\dot{b}$), must be accounted for in the model.

These measurements of range and range rate can be coupled with additional measurements to estimate receiver position and time. Accessory measurements include satellite position, satellite velocity, Signal-to-Noise Ratio (SNR), and Carrier-to-Noise ratio (C/N_0). For GPS, the satellite position and velocity are transmitted as orbital elements in the ephemeris of the navigation message. Additionally, TLE files and precise ephemeris are available online for post-processing applications. The SNR and C/N_0 measurement is a metric of the the quality of the signal as a function of noise. The fundamental difference between the two is the SNR is calculated before modulation, and the C/N_0 is determined after modulation. Further details regarding these metrics can be found in [40, 41].

2.2.3 Estimation Techniques: Least Squares and the Kalman Filter

For navigation applications, the GPS measurements described are used to estimate a receiver states, such as PVT. However, due to noise and environmental effects, these measurements contain error, which must be considered in the estimator. Additionally, many navigation systems incorporate additional sensors, such as Inertial Measurement Units (IMU's), radar, and camera vision. For the sensor suite to operate cohesively, the measurements must be *fused* and *filtered*. The estimation processes presented in this section are recursive Least Squares (LS), recursive Weighted Least Squares (WLS), and the Kalman Filter.

The recursive LS estimation framework is an iterative solver to estimate receiver states. In this architecture, the system is assumed to be linear and time-invariant. Nonlinear equations must be linearized about an operating point, which is typically chosen to be the current estimate of the state vector, and is often referred to as the *Newton-Raphson method*. The fundamental idea of the LS solution is to iteratively solve a system of equations to minimize the magnitude of the errors, or residuals. In this section, the implementation of the algorithm is discussed, and further information regarding the derivation and theory can be found in [38]. For clarity, measurements are denoted with *tilde*, and state estimates are denoted with *hat*.

The LS algorithm is constructed to solve the generic system model expressed as:

$$\mathbf{y} = \mathbf{H}\mathbf{x}, \tag{2.7}$$

where **y** is the measurement vector of size $(m \times 1)$ in Equation (2.8),

$$\mathbf{y} = \begin{bmatrix} y_1 \\ y_2 \\ \vdots \\ y_m \end{bmatrix} \tag{2.8}$$

x is the state vector of size $(n \times 1)$ in Equation (2.9),

$$\mathbf{x} = \begin{bmatrix} x_1 \\ x_2 \\ \vdots \\ x_n \end{bmatrix} \tag{2.9}$$

and **H** is the transformation matrix from the state to the measurement domain, or state-to-measurement mapping matrix of size $(m \times n)$. In order to minimize the square root of the sum of the errors squared, Equation (2.7) can be expressed as a function of measurement and state residuals, which is shown in Equation (2.10),

$$\delta\mathbf{y} = \mathbf{H}\delta\mathbf{x} \tag{2.10}$$

where $\delta\mathbf{y}$ and $\delta\mathbf{x}$ are defined in Equation (2.11) and Equation (2.12), respectively.

$$\delta\mathbf{y} = \begin{bmatrix} \tilde{y}_1 - \hat{y}_1 \\ \tilde{y}_2 - \hat{y}_2 \\ \vdots \\ \tilde{y}_m - \hat{y}_m \end{bmatrix} \tag{2.11}$$

$$\delta\mathbf{x} = \begin{bmatrix} \Delta\hat{x}_1 \\ \Delta\hat{x}_2 \\ \vdots \\ \Delta\hat{x}_n \end{bmatrix} \tag{2.12}$$

For a linear, time-invariant system, the state-to-measurement mapping matrix can be populated directly from the measurements and is considered to be constant. However, for a nonlinear measurement model, such as those presented in Equation (2.3) and Equation (2.6), the mapping must be linearized about the current state estimates. This linearization can be achieved by calculating the Jacobian of the measurement model as shown in Equation (2.13).

$$\mathbf{H} = \begin{bmatrix} \frac{\partial y_1}{\partial x_1} & \frac{\partial y_1}{\partial x_2} & \cdots & \frac{\partial y_1}{\partial x_n} \\ \frac{\partial y_2}{\partial x_1} & \frac{\partial y_2}{\partial x_2} & \cdots & \frac{\partial y_2}{\partial x_n} \\ \vdots & \vdots & \ddots & \vdots \\ \frac{\partial y_m}{\partial x_1} & \frac{\partial y_m}{\partial x_2} & \cdots & \frac{\partial y_m}{\partial x_n} \end{bmatrix}_{\mathbf{x}=\hat{\mathbf{x}}} \tag{2.13}$$

Equation (2.10) can be rearranged to solve for the state residual vector by taking the inverse of the state-to-measurement mapping matrix, resulting in Equation (2.14).

$$\delta\mathbf{x} = \mathbf{H}^{-1}\delta\mathbf{y} \tag{2.14}$$

However, this operation is only valid if the number of states is equal to the number of measurements (i.e. $m = n$), as $\mathbf{H}$ must be invertible. Misra and Enge define a solution to this issue using the orthogonality principle, which is shown in Equation (2.15) [38].

$$\delta \mathbf{x} = (\mathbf{H}^T\mathbf{H})^{-1}\mathbf{H}^T\delta \mathbf{y} \tag{2.15}$$

To improve performance of the estimation algorithm, knowledge of the measurement quality can be factored into the solution by *weighting* the measurements. These measurement weights are commonly derived from SNR, C/N_0, or satellite geometry metrics, such as elevation angle. Assuming the measurement uncertainties are uncorrelated with each other, the weighting matrix **W** can be expressed as:

$$\mathbf{W} = \begin{bmatrix} w_1 & 0 & \dots & 0 \\ 0 & w_2 & \ddots & \vdots \\ \vdots & \ddots & \ddots & 0 \\ 0 & \dots & 0 & w_m \end{bmatrix}, \tag{2.16}$$

where $[w_1, w_2, \dots, w_m]$ are the weights assigned to each measurement in $\delta\mathbf{y}$. The measurement weighting matrix can be incorporated into the Equation (2.15) as is shown in Equation (2.17),

$$\delta \mathbf{x} = (\mathbf{H}^T\mathbf{W}\mathbf{H})^{-1}\mathbf{H}^T\mathbf{W}\delta \mathbf{y} \tag{2.17}$$

yielding the WLS state residual vector.

Aside from estimating the values for each of the states of interest, the LS and WLS algorithms can also provide insight into the certainty of the estimates. This information is calculated and presented in the form of a covariance matrix, which is shown in Equation (2.18),

$$\mathbf{P} = (\mathbf{H}^T\mathbf{H})^{-1} = \begin{bmatrix} \sigma_{x_1}^2 & \sigma_{x_1x_2} & \dots & \sigma_{x_1x_n} \\ \sigma_{x_1x_2} & \sigma_{x_2}^2 & \ddots & \sigma_{x_2x_n} \\ \vdots & \ddots & \ddots & \vdots \\ \sigma_{x_1x_n} & \sigma_{x_2x_n} & \dots & \sigma_{x_n}^2 \end{bmatrix} \tag{2.18}$$

where the diagonal terms are the statistical variance of each state estimate, and the off-diagonal terms are the covariances. The LS and WLS algorithm can be executed with the following steps, which are visualized in Figure 2.6.

1. **Generate Initial State Estimates**

   Prior to processing the measurements, the initial system states must be either calculated or known *a priori*. While it is not necessary for the initial conditions to be perfectly-known, initialization outside of the general solution can cause the algorithm to converge to a local minima outside of the correct solution space in the nonlinear case.

2. **Compute State-to-Measurement Mapping Matrix**

   For nonlinear systems, the state-to-measurement mapping matrix must be updated at each iteration to reflect the most recent state estimates. For linear systems, this step can be ignored, as the mapping matrix remains constant and can be determined before the regression is performed.

3. **Calculate Measurement Residual Vector**

   For each iteration, the objective is to drive the measurement error vector to zero. Equation (2.11) can be used to update the measurement error as a function of the state estimates.

4. **Calculate State Residual and Update Full State Vector**

   After the measurement residual vector is computed, each of the terms on the right side of Equation (2.15) or Equation (2.17) are known, and the state residual vector in Equation (2.12) can be calculated. The residual vector should then be added to the full state vector to track the convergence of the estimate, which is shown in Equation (2.19).

   $$\hat{\mathbf{x}} = \hat{\mathbf{x}} + \delta\hat{\mathbf{x}} \tag{2.19}$$

5. **Assess the Convergence of the State Estimate**

   Once the full state vector is updated, the convergence of the recursive least squares algorithm should be tested against a pre-defined tolerance, T, which is shown in Equation (2.20).

$$||\delta\hat{\mathbf{x}}|| < T \tag{2.20}$$

   The value of T should be small enough to ensure convergence but large enough to be achievable in the presence of measurement uncertainty.

6. **Compute Estimate Uncertainty**

   Finally, after the solution has converged, the state covariance matrix can be computed to gauge the quality of each estimate as shown in Equation (2.18).

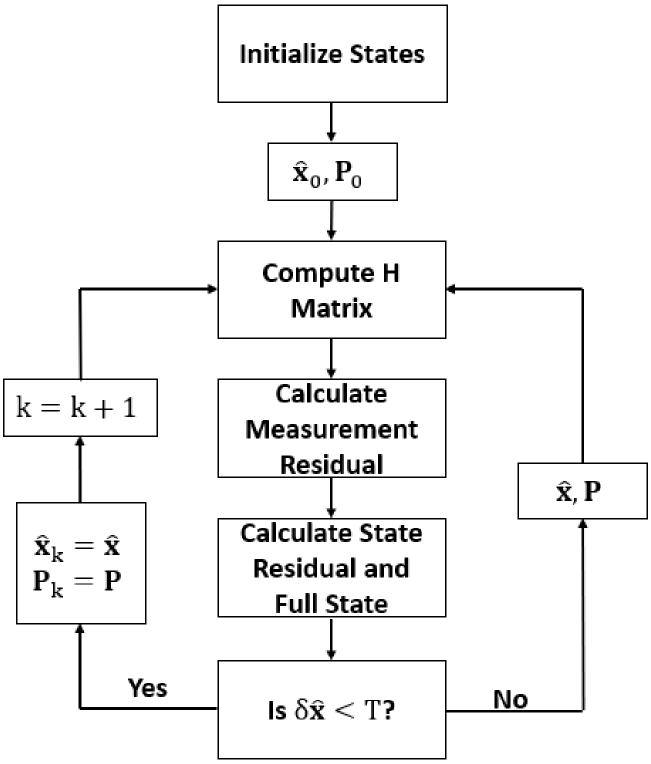

Figure 2.6: Least Squares Estimation Flowchart

The LS method is a highly-capable solution for estimating the instantaneous states of a system, such as a PVT solution with GPS measurements at a single instance. However, when fused with additional sensors or models, the estimator does not include the measurements or stochastic noise parameters necessary to fuse the available information for a dynamic solution. The Kalman Filter provides a framework to combine measurements from multiple sensor sources functioning at various update rates to estimate the states and state covariance of a system as it is changing.

For linear, time-invariant systems, the Kalman Filter is an optimal estimator. The term *optimal* refers to the the filter calculating an ideal observer gain to weight the measurements as a function of the process and measurement noise to minimize the estimation error. In this thesis, only the fundamental equations and implementation are presented. Further reading regarding the derivations and additional implementations can be found in [38, 42, 43].

The Kalman Filter contains two primary components: a time update (prediction phase) and a measurement update (correction phase). The sequence of the estimator can be best explained with an example of a navigation algorithm composed of a dynamic model updating at 100 Hz and a generic positioning sensor operating at 1 Hz. In this example, the dynamic model is updated significantly faster than GPS, but due to inherent noise in the system, its errors grow unbounded in time. However, for short periods, the model provides useful state information to the system. By coupling this model with a positioning sensor, a fusion algorithm is developed, which leverages both components to estimate the states at 100 Hz and *fix* the position at each 1 Hz sensor update. Additionally, the model can be used to reject errant measurements from the sensor, increasing the fidelity and robustness of the estimator.

The described system can be expressed in the discrete state space form:

$$\mathbf{x}_k = \mathbf{A}\mathbf{x}_{k-1} + \mathbf{B}_w\varepsilon, \tag{2.21}$$

where $\varepsilon \sim N(0,\ \sigma_\varepsilon^2)$, and Equation (2.22) defines the sensor measurement mapping,

$$\mathbf{y}_k = \mathbf{H}\mathbf{x}_k + \eta \tag{2.22}$$

in which $\eta \sim N(0,\, \sigma_\eta^2)$. In these equations, $\mathbf{A}$ is the state transition matrix, $\mathbf{B}_w$ is the dynamics noise input matrix, ε is the process noise, $\mathbf{H}$ is the state-to-measurement mapping matrix, and η is the measurement noise. For the example system, the dynamic model is defined as the time update, as it *predicts* the states of the system, and the positioning sensor is defined as the measurement update, as it *corrects* the states propagated in the time update. Along with the states, the Kalman Filter also propagates the uncertainty of the estimates as a state covariance matrix. The states and covariance are updated as a function of the noise in the prediction and correction, both of which are assumed to be zero mean, Gaussian distributions.

For nonlinear systems, such as the measurement models presented in Equation (2.3) and Equation (2.6), the models must be linearized about the current state estimate, but the estimator can no longer be considered *optimal*. The nonlinear implementation of the Kalman Filter is called the Extended Kalman Filter (EKF). Although not mathematically optimal, the EKF provides a simple and robust estimation framework, especially in the presence of model and measurement uncertainty.

The Kalman Filter and EKF can be implemented with the following process, which is depicted in Figure 2.7. Again, *tilde* notation is used to denote a direct measurement, *hat* notation is used to denote a filter estimate, and k defines the discrete instance in time. Additionally, the *minus* and *plus* superscripts are used to define the time and measurement update, respectively.

1. **Generate Initial State Estimates**

   Similarly to the LS solution, the Kalman Filter states and covariance must be initialized. For the nonlinear EKF, the initial conditions must be close to the actual states in order for the solution to converge correctly. A popular approach to this issue is to utilize the LS solution to estimate the states with a set of measurements prior to executing the filter.

2. **Time Update**

   The time update is composed of two parts: the state and covariance propagation, which are shown in Equation (2.23) and Equation (2.24), respectively,

$$\hat{\mathbf{x}}_k^- = \mathbf{A}\hat{\mathbf{x}}_{k-1}^+ + \mathbf{B}_w \epsilon \tag{2.23}$$

$$\mathbf{P}_k^- = \mathbf{A}\mathbf{P}_{k-1}^+ \mathbf{A}^T + \mathbf{Q} \tag{2.24}$$

   where **Q** is the process noise covariance matrix. Typically, the time update consists of a sensor or model that can be updated faster than the sensor in the measurement update. For initialization, the state and covariance with the *plus* superscript should be substituted for the system's initial conditions.

   In the case of nonlinear system dynamics defined as:

$$\hat{\mathbf{x}}_k^- = \mathbf{f}(\hat{\mathbf{x}}_{k-1}^+) = \begin{bmatrix} f_1(\hat{\mathbf{x}}_{k-1}^+) \\ f_2(\hat{\mathbf{x}}_{k-1}^+) \\ \vdots \\ f_n(\hat{\mathbf{x}}_{k-1}^+) \end{bmatrix}, \tag{2.25}$$

   the state transition matrix must be linearized by calculating the Jacobian, and evaluating the matrix at the most recent update, which is shown in Equation (2.26).

$$\mathbf{A} = \begin{bmatrix} \frac{\partial f_1}{\partial x_1} & \frac{\partial f_1}{\partial x_2} & \cdots & \frac{\partial f_1}{\partial x_n} \\ \frac{\partial f_2}{\partial x_1} & \frac{\partial f_2}{\partial x_2} & \cdots & \frac{\partial f_2}{\partial x_n} \\ \vdots & \vdots & \ddots & \vdots \\ \frac{\partial f_n}{\partial x_1} & \frac{\partial f_n}{\partial x_2} & \cdots & \frac{\partial f_n}{\partial x_n} \end{bmatrix}_{\mathbf{x}=\hat{\mathbf{x}}} \tag{2.26}$$

3. **Measurement Update**

   The measurement update of the Kalman Filter consists of three major components: the Kalman gain, measurement state update, and measurement covariance update. First, the

Kalman observer gain (**L**) is calculated as a function of the state covariance matrix, state-to-measurement mapping matrix, and measurement noise covariance matrix (**R**), which is shown in Equation (2.27).

$$\mathbf{L} = \mathbf{P}_k^- \mathbf{H}^T (\mathbf{H}\mathbf{P}_k^- \mathbf{H}^T + \mathbf{R})^{-1} \tag{2.27}$$

For the linear case, this gain is *optimal*, in the sense that the filter computes an ideal gain to balance the process noise, which is incorporated into $\mathbf{P}_k^-$, and the measurement noise.

The second step in the measurement update is to propagate the state vector. The states are estimated as a function of the time update state vector, Kalman gain, measurement vector ($\tilde{\mathbf{y}}$), and measurement estimate vector ($\hat{\mathbf{y}}$), which is shown in Equation (2.28).

$$\hat{\mathbf{x}}_k^+ = \hat{\mathbf{x}}_k^- + \mathbf{L}(\tilde{\mathbf{y}} - \hat{\mathbf{y}}) \tag{2.28}$$

Finally, the state covariance matrix can be calculated as Equation (2.29),

$$\mathbf{P}_k^+ = (\mathbf{I} - \mathbf{L}\mathbf{H})\mathbf{P}_k^- \tag{2.29}$$

where **I** is an identity matrix with dimensions $n \times n$.

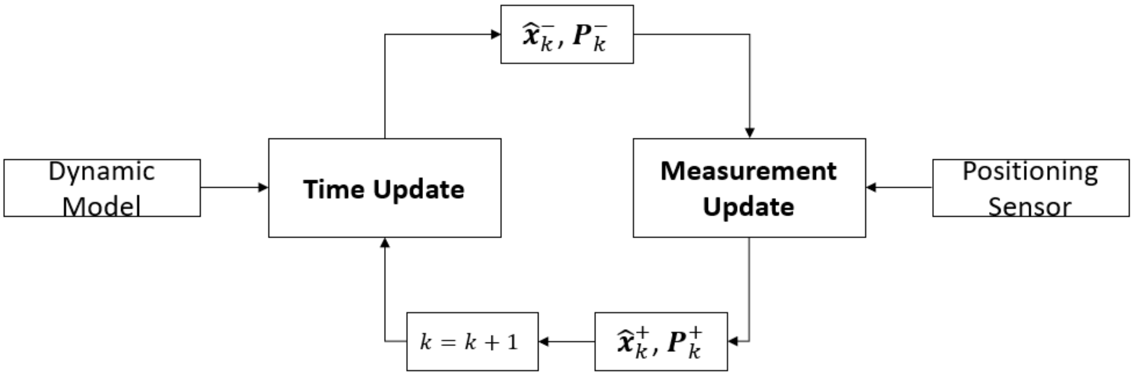

Figure 2.7: Kalman Filter Estimation Flowchart

2.2.4 Kalman Filter Coupling Architectures

For satellite navigation applications, the Kalman Filter can be implemented in three frameworks: loosely-, tightly-, and deeply-coupled. For each of these configurations, the time update remains the same, but the level of GPS integration changes. For demonstration purposes, the remainder of this section considers a navigation sensor setup consisting of an Inertial Navigation System (INS) for the time update, and GPS for the measurement update.

A loosely-coupled GPS/INS integration is the simplest coupling scheme and utilizes a solution-level measurement update. The INS prediction and GPS correction are incorporated into the filter as navigation states, and the collaborative architecture performs significantly better than individual GPS and INS solutions. The loosely-coupled architecture is depicted in Figure 2.8. The measurement noise can be modeled as a function of the GPS receiver position and velocity state estimate uncertainties, which are often reported from an internal Kalman Filter in the receiver module. One of the advantages to the loosely-coupled scheme is a ”black box” approach can be taken when integrating the GNSS receiver module [44]. Under this assumption, only the state and covariance outputs from the receiver must be considered, and signal tracking and quality can be ignored. The primary drawback to the loose integration is a full navigation solution is required for each measurement update, resulting in poor filter performance under conditions where Radio Frequency (RF) signals are degraded.

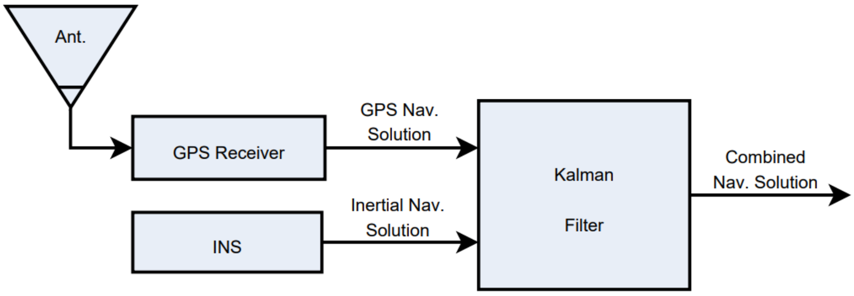

Figure 2.8: Loosely-Coupled GPS/INS Kalman Filter Architecture [45]

In a tightly-coupled integration, the GNSS receiver module tracks the incoming signal and generates raw observables, such as pseudorange and Doppler shift. The Kalman Filter implements the measurements for the navigation solution, where the measurement noise can be determined from signal quality metrics, such as C/N_0 and elevation angle. The tightly-coupled architecture is depicted in Figure 2.9. The primary advantage to the this coupling is the filter's ability to utilize individual satellite measurements when a full navigation solution is not available or observability challenges arise, which could be caused by poor signal quality, environmental factors, or high dynamic scenarios [46].

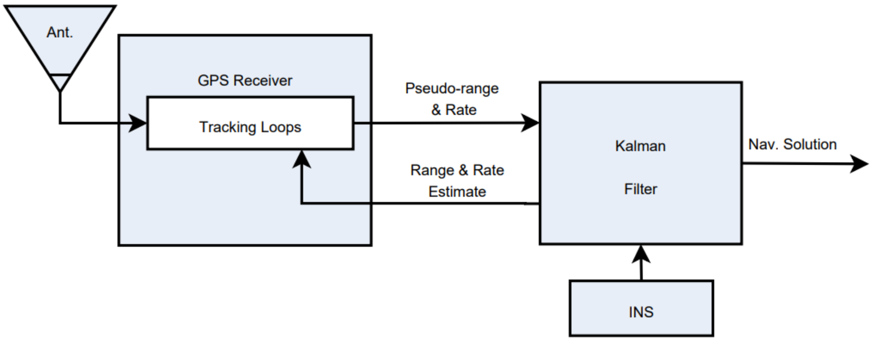

Figure 2.9: Tightly-Coupled GPS/INS Kalman Filter Architecture [45]

The deeply-coupled Kalman Filter is the lowest level of integration, where the filter utilizes detector signals (I's and Q's), or correlator samples, to update the observables and the navigation states [47]. The deeply-integrated system is based around vector tracking, in which satellite signals are processed collectively, and PVT estimation is accomplished simultaneously. The primary benefits to vector tracking is the ability to operate with lower signal strengths and higher dynamics [48, 49]. A diagram of the deeply-coupled GNSS/INS architecture is shown in Figure 2.10.

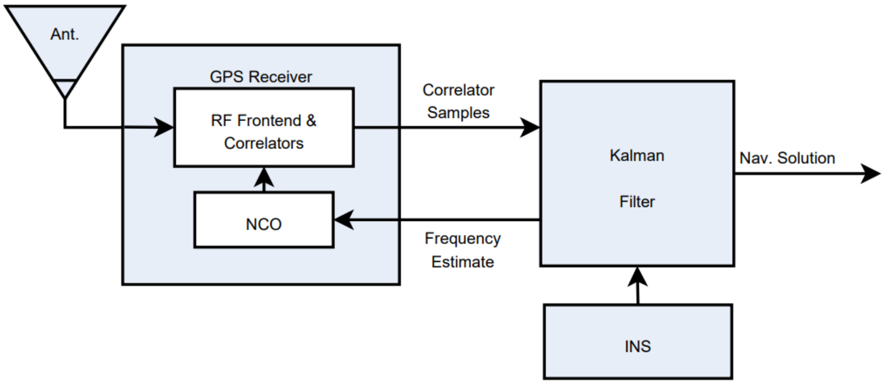

Figure 2.10: Deeply-Coupled GPS/INS Kalman Filter Architecture [45]

2.3 Basics of GPS Navigation

As is previously stated, the primary role of GPS is to provide accurate position, navigation, and timing information to users. From the previous section, measurements of range, range rate, satellite position, and satellite velocity are the bare minimum required to form these solutions. In this section, the method with which satellites communicate this information with receivers is discussed. First, the signal properties are briefly presented. Next, the vulnerabilities of GPS are considered. Finally, the conditions for accurate navigation solutions are discussed. While not directly in the scope of this thesis, basic knowledge of GPS signals and their weakness is necessary to understand the motivation for this research.

2.3.1 Signal Properties

GPS satellites broadcast data containing PVT states of the satellites. This information is transmitted at three carrier frequencies: L1 (1575 MHz), L2 (1227 MHz), and L5 (1176 MHz). Each satellite has an unique Pseudo-Random Noise (PRN) sequence, which receivers use to track and differentiate the incoming signals. The navigation data is modulated onto the signal in the ephemeris, which contains orbital parameters to calculate satellite position and velocity, timing, and satellite health information.

GPS receiver antennas operate passively, implying the user equipment communicates no information to the space segment. The downlink transmissions are Code-Division Multiple Access (CDMA), meaning the satellites broadcast continuous messages, which are differentiated at the receiver-level by the unique, modulated PRN codes. Therefore, GPS receivers can continuously track each satellite in view simultaneously, the importance of which will be discussed in the next section. Further information regarding the GPS signal structure can be found in [38, 50].

2.3.2 GPS Vulnerabilities

Generally, GPS is capable of providing sufficient positioning and timing information for a variety of users. However, conditions exist which degrade the fidelity of the RF signals, and therefore the navigation solution. In clear, open-sky environments, atmospheric effects, mainly the ionosphere, are the greatest source of error in GPS performance. The altitude of the ionosphere ranges between $50 - 1500$ kilometers, where electrons in the atmosphere obstruct the signal path [51]. In this region, the ionosphere introduces a delay in the transit of the signal. In severe cases, ionospheric effects contribute up to 100 meters of error in range measurements [52].

The primary vulnerability of GPS is apparent in scenarios where the satellite-to-receiver signal path is obstructed. To illustrate, Figure 1.1 depicted the network synchronization capabilities of satellite navigation services. However, Figure 2.11 demonstrates how buildings are interfering with the connection to System 2. This scenario is commonly referred to as an *urban canyon*, which pose a significant threat to GPS capabilities. Similarly, GPS performance is degraded for indoor applications and in heavy foliage.

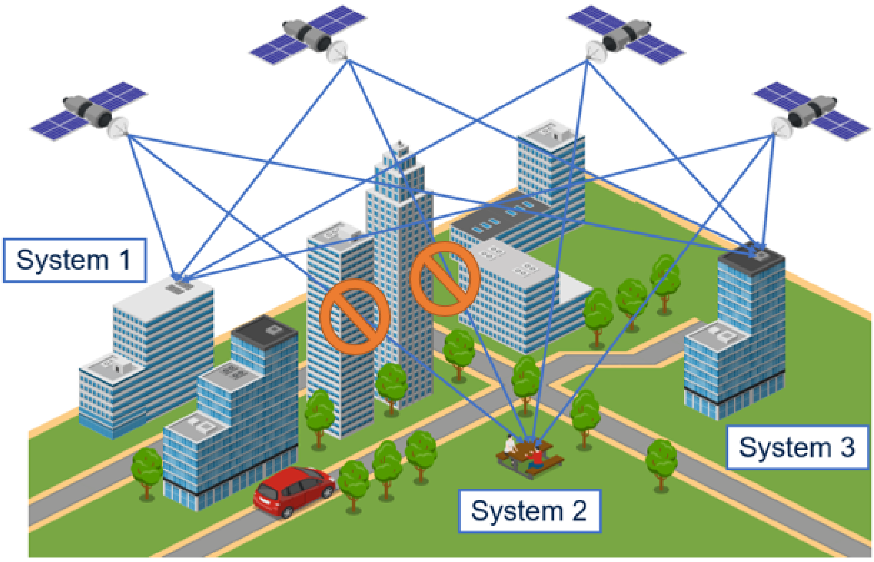

Figure 2.11: Obstructed Remote Network Timing Synchronization

Obstructions to the GPS signal path have a significant impact on the accuracy of the system. This is largely due to the received signal power. As with any signal, GPS is susceptible to propagation loss, which is defined as:

$$P_L = P_T - P_R, \tag{2.30}$$

where P_L is the power loss, P_T is the transmitted power, and P_R is the received power [53]. Fundamentally, path loss can be modelled as a function of distance and frequency, which is demonstrated in [54, 55]. GPS satellites orbit at approximately 20,200 kilometers [39]. Coupling the orbital altitude with free space path loss, the signals are critically weak at the receiver antenna. Therefore, additional sources of attenuation introduced by obstructions to the line-of-sight vector, including buildings, walls, and foliage, negatively impacts measurement quality and can result in a loss of signal.

In the event that a receiver is unable to track an incoming signal, observability of the navigation solution can be at risk. The observability of PVT solution can be assessed with the state transition matrix (**A**) and the state-to-measurement mapping, or observation, matrix (**H**) defined in Equation (2.26) and Equation (2.13), respectively. For an estimator to be fully-observable, the observability matrix (**O**) must be full rank, which is shown in Equation (2.31) and Equation (2.32).

$$\mathbf{O} = \begin{bmatrix} \mathbf{H} \\ \mathbf{HA} \\ \vdots \\ \mathbf{HA}^{n-1} \end{bmatrix} \tag{2.31}$$

$$rank(\mathbf{O}) = n \tag{2.32}$$

As is shown in Chapter 3, for position, velocity, and timing estimation, measurements from a minimum of four satellites are required for each update epoch. The GPS system is designed such that at least four satellites are in view from anywhere on Earth, therefore providing an observable solution [39]. However, blockage or outage can compromise observability and affect users.

2.4 Iridium Satellite Time and Location Navigation

Combining the capabilities of GPS and its integration into technology, it is worthwhile to consider alternative space systems that may provide a complement or backup to PNT services. Recently, great interest has developed in the navigation capabilities LEO satellite systems, namely the Iridium constellation, can provide. In this section, an overview of Iridium constellation is presented, including system properties, advantages and disadvantages when compared to GPS, and signal properties. For the purposes of this thesis, the focus of this discussion will revolve around the timing aspect of the navigation solution.

2.4.1 Overview of the Iridium Constellation

The Iridium constellation was developed by Motorola as a satellite communications network. The name of the constellation was derived from the plan to utilize 77 satellites in the space system, which is also the atomic number of the iridium element. However, after design changes, only 66 satellites were necessary, which were sent into orbit between the initial launch in 1996 and beginning of operation in 1998 [56]. Although not intended for navigation usage, updates to the space segment have enabled significant strides in LEO navigation, particularly in timing.

The 66 satellites are oriented in 6 polar, circular orbital planes at an altitude of 780 kilometers and inclination angle of 86.4°. The satellites broadcast spot beam signals, which are shown in Figure 2.12, and yield greater signal power than omnidirectional systems, such as GPS. Each satellite is equipped with three phased array, L-band antennas which individually generate 16 beams, totalling 48 per satellite and divide the total satellite footprint into cells. Each of the beams are assigned a portion of the system's frequency spectrum, enabling spatially-separated signals to re-use center frequencies in a manner that avoids co-channel interference. Combining the 48 spot beams per satellite, the radial footprint of each satellite is approximately 2,209 kilometers [57].

The Iridium constellation operates in two frequency bands: K and L. The K-band serves as an uplink, downlink and crosslink, which utilize the frequencies: 27.5-30.0 GHz, 18.8-20.2

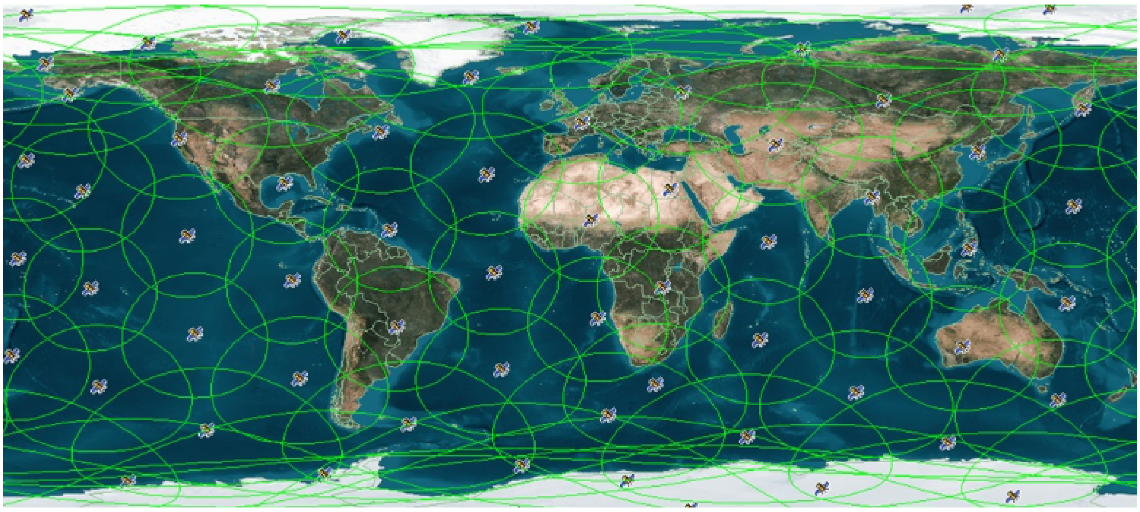

Figure 2.12: Iridium Spot Beam Coverage Map [58]

GHz, and 22.55-23.55 GHz, respectively. The channels are transmitted and received with both Time- and Frequency-Division Multiple Access (TDMA/FDMA) and are described in depth in [56]. For the applications presented in this thesis, the primary functions of the K-band are to connect nearby satellites and transmit data between Iridium's ground segment and the space vehicles. Inter-satellite communications ensure global coverage and reduce ground segment requirements, and the downlink/uplink serves to communicate information within the system to maintain functionality.

The Iridium communications user segment utilizes the L-band, which operates between 1616-1625.5 MHz and are also differentiated with TDMA/FDMA. In the TDMA architecture, the communications transmissions are differentiated with four slots for both the uplink and downlink, totalling 90-millisecond frames. The FDMA scheme divides the total bandwidth of the signal into 240 channels of 41.67 kHz slots, which are used to service users within the area of each spot beam [59].

2.4.2 Iridium STL Signal

Since its launch, in addition to communications, the Iridium constellation has evolved to broadcast navigation information from the satellites. The service is termed *Satellite Time and Location*, or STL, and is maintained and operated by Satelles, Inc. The STL message is transmitted as a downlink simplex channel in the L-band and operates with Time-Division

Duplexing (TDD). Simply stated, each satellite broadcasts satellite PVT information with signal *bursts*, as opposed to a continuous signal, such as GPS. Since the constellation provides global coverage, users are guaranteed to have at least one Iridium satellite visible are any time, ensuring that navigation information can be received.

When comparing STL to GPS, several advantages can be deduced, most of which can be derived from the relative satellite altitude. Equation (2.33) demonstrates that Iridium satellites orbit 26 times closer to Earth's surface than GPS.

$$\frac{alt_{GPS}}{alt_{STL}} = \frac{20200\,km}{780\,km} \approx 26:1 \tag{2.33}$$

At first glance, orbital altitude may seem insignificant for navigation applications. However, following three primary benefits can be drawn.

1. **Signal Strength**

   With lower orbital altitudes, signal attenuation due to free space path loss is reduced. Researchers estimates the STL signal to be approximately 1000 times stronger than GPS, significantly improving solution resiliency, especially in the presence of physical or electromagnetic obstructions [60].

2. **Relative Motion**

   The orbital period of Iridium satellites are approximately 100 minutes, compared to 12 hours for GPS [60]. Coupling the satellite velocity with the reduced range between the transmit and received antenna, the line-of-sight vector between the satellite and receiver changes rapidly, resulting in greater geometric diversity. In the example presented in Figure 2.11, an Iridium satellite would move across the sky faster than GPS, reducing the time of signal obstruction.

3. **Doppler Navigation**

   Aside from the STL signal, much of the prior art in LEO navigation is accomplished with Doppler navigation, which, instead of pseudorange, utilizes the Doppler shift measurements as a positioning approach. This method is feasible due to the rapid changes to satellite geometry, which will be demonstrated in Chapter 3.

While the Iridium STL signal is appealing for positioning and timing applications, the original concept was designed for communications, not navigation. Therefore, the inherent qualities in the system pose challenges for PNT estimation. Perhaps the greatest challenge in navigation with STL is observability. As previously discussed, for an observable position and timing solution, at least 4 satellites must be in view for each estimation epoch. Combining the orientation of the satellites and duplexing of the signal propagation, STL receivers only receive data from a single satellite at each burst, even when multiple satellites are in view. This challenge cannot be overlooked when assessing the feasibility of utilizing the STL signal for certain applications.

Navigation solutions can be augmented based on knowledge of a receiver's dynamic state. In dynamic scenarios, single-antenna, satellite-based estimation algorithms must estimate position, velocity, clock bias, and clock drift, totaling 8 states. However, if a receiver is known to be static, the velocity can be omitted from the state vector, resulting in 5 states. Furthermore, if a static receiver position is known, for timing applications, only a receiver clock bias and clock drift may be estimated from the pseudorange and pseudorange rate, respectively. In this thesis, only the timing of a static receiver is considered.

To improve observability, when estimating the position and time of a static receiver at a known location, measurements from Iridium satellites can be *batched* in time. With this method, measurements are grouped together and combined in the navigation solution for each update epoch. While observability can be achieved mathematically, short batch windows often result in poor satellite geometry, and therefore large uncertainty in the solution. While larger batch sizes can improve geometry, the clock dynamics are effectively averaged, yielding error in the state estimates. The following chapter applies the navigation principles to the STL data message for timing estimation of a receiver at a known and unknown position, and timing results and analysis are shown.

2.5 Conclusions

This chapter presented a concise overview of satellite navigation and timing with GPS and Iridium STL. First, a brief history of GPS and an overview of navigation principles, including coordinate frames, measurements, and estimation techniques, were discussed. Next, system properties and vulnerabilities of GPS were considered. Finally, the Iridium constellation and the STL signal were presented, and various advantages and disadvantages of the system were described.

Chapter 3

Receiver Timing State Estimation Study

3.1 Introduction and Theory

In Chapter 1, it was emphasized that numerous government, industrial, and personal systems utilize GPS timing capabilities for operation. It is also noted that GPS outages not only impair the functionality of these systems, but also pose a risk to public safety. The chapter also discussed prominent timing metrics, including GPS time. Chapter 2 provided a high-level overview of the GPS system and presented pseudorange and pseudorange rate measurement models, both of which are dependent on precise timing in both the space and user segment. This chapter aims to explain the correlation between satellite navigation and accurate timing, derive estimation algorithms which can be used to maintain time, and implement these algorithms with live-sky data collected with a variety of hardware configurations.

Satellite-based timing solutions provide systems with the ability to maintain accurate time, which can be traced to UTC. For example, financial institutions rely on these services for transaction timestamping, since clients are generally not equipped with local, disciplined atomic oscillators. The primary benefit of GPS timing is the ability for users to maintain the accuracy of atomic oscillators, without the need for the clock itself. In this thesis, satellite-based timing algorithms are applied to the Iridium constellation, and the performance is evaluated with a statistical analysis of the estimated receiver clock states. The pseudorange measurement calculation from Section 2.2.2 can be used to extract GPS time at the receiver, which is rewritten in Equation (3.1) for convenience.

$$\tilde{\rho} = c(\tilde{t}_{RCVR} - t_{SV}) \tag{3.1}$$

GPS satellites are equipped with highly stable, atomic oscillators, which are disciplined by the ground segment. For this work, it is assumed that Iridium network timing is also high-fidelity, and errors inherent to the system are neglected. However, the receiver clock error cannot be neglected, and therefore must be estimated in the measurement model, which is shown in Equation (3.2).

$$\hat{\rho} = r + c\hat{b} + \varepsilon_\rho \tag{3.2}$$

To calculate the actual received time, the estimated receiver clock bias ($\hat{b}$) must be combined with the measured receiver time ($\tilde{t}_{RCVR}$), resulting in Equation (3.3) and Equation (3.4).

$$\tilde{t}_{RCVR} = \hat{t}_{RCVR} + \hat{b} \tag{3.3}$$

$$\hat{t}_{RCVR} = \tilde{t}_{RCVR} - \hat{b} \tag{3.4}$$

Solving Equation (3.1) for the received time measurement and substituting Equation (3.3), Equation (3.5) and Equation (3.6) models the actual time of the receiver as a function of the estimated and measured states.

$$\tilde{\rho} = c(\tilde{t}_{RCVR} - t_{SV}) \rightarrow \tilde{t}_{RCVR} = t_{SV} + \frac{\tilde{\rho}}{c} \tag{3.5}$$

$$\hat{t}_{RCVR} = t_{SV} + \frac{\tilde{\rho}}{c} + \hat{b} \tag{3.6}$$

A similar process can be applied to calculate the corrected receiver oscillator frequency error, or clock drift. The pseudorange rate measurement calculation is shown in Equation (3.7),

$$\tilde{\dot{\rho}} = \frac{c}{f_c}\tilde{f}_d \tag{3.7}$$

and the Doppler shift is calculated as function of the signal center frequency and the measured receiver oscillator frequency in Equation (3.8).

$$\tilde{f}_d = f_c - \tilde{f}_r \tag{3.8}$$

Assuming the receiver velocity is known or zero, the pseudorange rate can be modelled as a function of the receiver clock drift, which is shown in Equation (3.9).

$$\hat{\dot{\rho}} = \dot{r} + c\hat{\dot{b}} + \varepsilon_{\dot{\rho}} \tag{3.9}$$

Similarly to the corrected receiver time in Equation (3.4), the measured and corrected receiver frequency can be calculated with Equation (3.10) and (3.11), respectively.

$$\tilde{f}_r = \hat{f}_r + \hat{\dot{b}} \tag{3.10}$$

$$\hat{f}_r = \tilde{f}_r - \hat{\dot{b}} \tag{3.11}$$

Solving Equation (3.8) for the received frequency measurement and substituting Equation (3.10), an estimate of the corrected receiver clock frequency can be calculated, which is shown in Equation (3.12) and Equation (3.13).

$$\tilde{f}_d = f_c - \tilde{f}_r \rightarrow \tilde{f}_r = f_c - \tilde{f}_d \tag{3.12}$$

$$\hat{f}_r = f_c - \tilde{f}_d + \hat{\dot{b}} \tag{3.13}$$

In this section, it is proven that only an estimated receiver clock bias and drift are necessary to correct the receiver oscillator and *steer* it to maintain accurate timing. However, inherent measurement errors result in uncertainty in the solution. For presentation, the remainder of this chapter gauges the timing performance of the filters with the estimate statistics of receiver clock bias and drift.

3.2 Data Collection Hardware

In order to examine the timing capabilities of the STL system, multiple data collection frameworks were constructed. In this section, the hardware and software components are discussed. Among these components are the STL receiver, internal and external oscillators, a GNSS timing reference station, and the data collection computer and software.

3.2.1 Jackson Labs Technologies STL-2600 Receiver

Considering the growing interest in LEO-based PNT, the threats to existing GNSS constellations, and the commonalities between the STL system and GPS, it is understandable that the navigation industry is eager to apply the Iridium network for timing solutions. As an early contributor, Jackson Labs Technologies, Inc. is the manufacturer of the STL-2600 (denoted by JL STL-2600), which is a newly-released, commercially-available STL timing receiver. The module was developed by Jackson Labs Technologies, Inc. in partnership with Satelles, Inc. and is capable of processing GPS L1 and STL data messages. The receiver module is shown in Figure 3.1, and its dimensions are 36 mm × 51 mm × 13 mm [61]. In this thesis, only the timing capabilities of the STL output are assessed, which are advertised to be of the nanosecond-level [62].

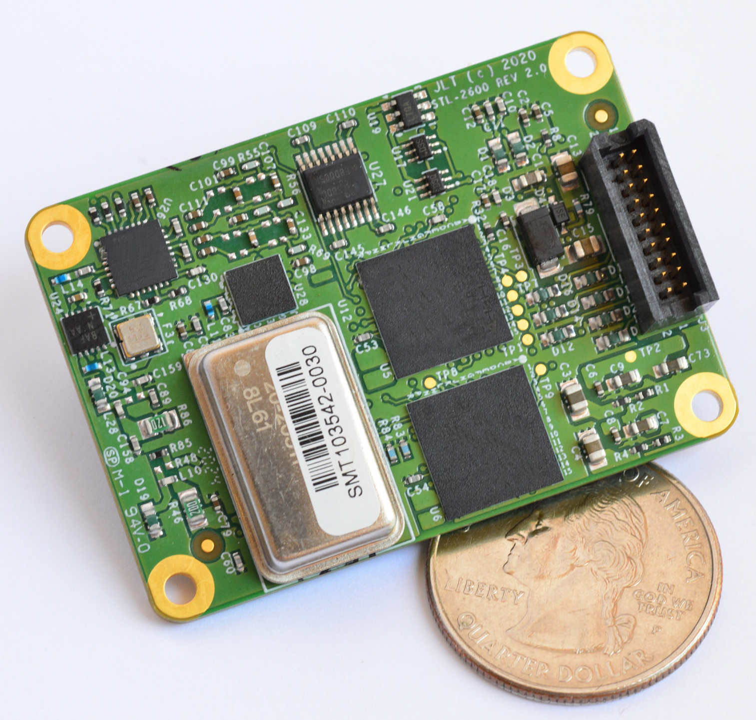

Figure 3.1: JL STL-2600 Receiver Module [61]

The JL STL-2600 board is equipped with a TCXO clock, and the frequency characteristics are described in Section 3.2.2. When locked to the incoming GPS or STL signal, the receiver oscillator is disciplined to GPS time. The module contains pins outputting direct 1-PPS and 1 MHz voltage signals and is capable of accepting timing references of the same type from external sources. For the timing state estimation portion of this thesis, the satellite states and measurements were outputted from the receiver board via USB connection, and the following measurements were extracted.

- ECEF Satellite Position [m]
- ECEF Satellite Velocity [m/s]
- Satellite Time [s]
- Pseudorange [m]
- Doppler Shift [Hz]
- Carrier-to-Noise Ratio [dB]
- Azimuth Angle [deg]
- Elevation Angle [deg]

For demonstration purposes, the direct outputs of the pseudorange and Doppler shift measurements are shown in Figure 3.2 and Figure 3.3, respectively. It may be noted that the pseudorange measurements are significantly larger than what may be expected from the orbital altitude of the satellites, which is further explained in Section 3.5. Another notable feature of the Iridium constellation is the large Doppler shift, which ranges between -40 and 40 kHz and can be used as a positioning source.

3.2.2 Receiver Oscillators

As previously discussed, one of the primary functions of satellite-based navigation is the user's ability to maintain nanosecond-level timing, even when the receiver is not disciplined with an atomic oscillator. However, it is not necessarily true that the quality of the receiver clock has no impact on the accuracy of the timing solution. Satellite-based navigation solutions are updated in epochs, implying gaps between estimates. In between these gaps or during outage periods, inherent noise and errors corrupt the 10 MHz reference signal, which is not steered

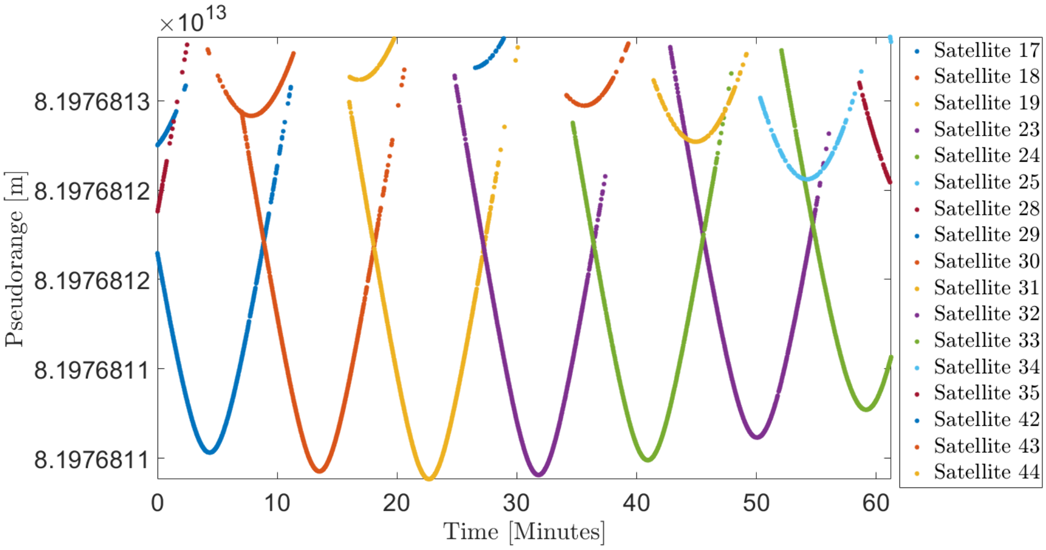

Figure 3.2: JL STL-2600 Pseudorange Measurements

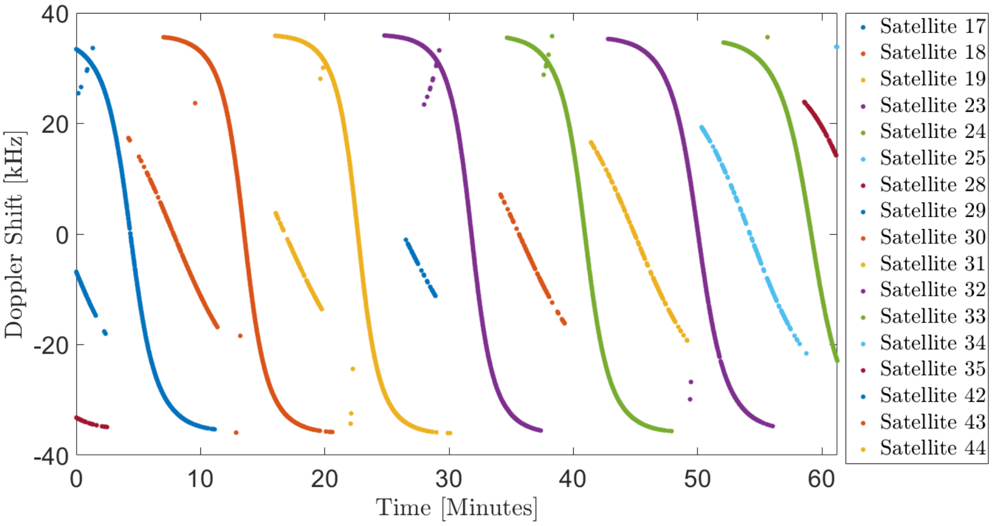

Figure 3.3: JL STL-2600 Doppler Shift Measurements

until the next update. Naturally, without a correction, the error in the receiver timing solution, or integral of the oscillator frequency, grows unbounded in time. Therefore, improving the quality of the receiver oscillator reduces the frequency error and time error growth rate.

The most prominent means of quantifying the accuracy and stability of clocks is through Allan variance analysis. Allan variance is a time domain representation of the phase and frequency noise associated with reference signals from oscillators [63]. This noise is represented as a statistical analysis of the fluctuations over a time window (also known as *clusters*), in which the deviation or variance are used for characterization. Allan variance results are typically displayed on a logarithmic-logarithmic plot, in which the x- and y-axes are the cluster size and Allan deviation, respectively [64]. Further explanation and derivations of the Allan variance can be found in [63, 65, 66], but they are beyond the scope of this thesis.

For this work, the primary takaways from Allan variance analysis are the noise coefficients derived from the deviation plots, which are shown in Table 3.1. These coefficients can be used to compute the power spectral densities of the continuous-time process noise, which are shown in Equation (3.14) and Equation (3.15) [67].

$$S_f \sim \frac{h_0}{2} \tag{3.14}$$

$$S_g \sim 2\pi^2 h_{-2} \tag{3.15}$$

These equations are needed to model the process noise in the discrete domain in Section 3.4.1.

Table 3.1: Typical Allan Variance Coefficients for TCXO and Rubidium Oscillators [68]

Timing Standard	$\mathbf{h}_0$	$\mathbf{h}_{-1}$	$\mathbf{h}_{-2}$
Low-Quality TCXO	2×10^{-19}	7×10^{-21}	2×10^{-20}
High-Quality TCXO	2×10^{-21}	1×10^{-22}	3×10^{-24}
Rubidium	2×10^{-22}	4.5×10^{-26}	1×10^{-30}

In both experimental results presented in this thesis, the on-board TCXO, which is conservatively implemented with the low-quality model in Table 3.1 and pictured on the board in Figure 3.1, is used for the majority of the data collections. To examine the effects of integrating an improved local oscillator, a Stanford Research Systems FS725 Rubidium Frequency Standard is incorporated into the receiver hardware. The rubidium oscillator used for this study is shown in Figure 3.4.

3.2.3 SecureSync Time and Frequency Reference System

The timing reference station used in data collection is the Safran SecureSync 2400 Time and Frequency Reference System, which is pictured in Figure 3.5. The server is equipped

Figure 3.4: Stanford Research Systems Model FS725 Rubidium Frequency Standard [69]

with an internal rubidium oscillator disciplined by a multi-GNSS receiver, which is capable of tracking GPS, Galileo, GLONASS, and BeiDou and outputting a 1-PPS and 10 MHz timing reference signal. The antenna is mounted on a roof of the GPS and Vehicle Dynamics Laboratory in Auburn, Alabama, and was also used to collect the STL data for this experiment. The server contains an internal, rubidium oscillator, which is highly-stable and advertised to keep accurate time to ± 15 nanoseconds. In the event of a GNSS outage, the 1-PPS timing output is reported to maintain sub-microsecond-level accuracy for up to 24 hours [70]. As the most accurate timing solution available for this thesis at the time of the data collection, the SecureSync reference station is used as truth for both experiments in this study.

Figure 3.5: Safran SecureSync 2400 Reference System [70]

3.2.4 Laptop and Software

For the first experiment, only data from the JL STL-2600 receivers were collected for post processing. Data was transmitted from the receivers to an HP Z-Book via USB connection. Within the computer, Linux-based, Robotic Operating System (ROS) C++ drivers were used to interface with the sensors and collect the STL data into bag files. Once collection was completed, the bag files were imported into MATLAB, parsed, and post-processed.

3.3 Hardware Configurations

To conduct the timing state estimation study, two hardware configurations were constructed. The first experimental setup consisted of a roof-mounted, GNSS/STL antenna, JL STL-2600 receiver, and collection computer. The receiver module's firmware was configured to only utilize data from the STL message to avoid GPS-aiding. The receiver was also configured to static mode, and a well-known antenna location was provided upon start-up. A diagram of the collection hardware is shown in Figure 3.6.

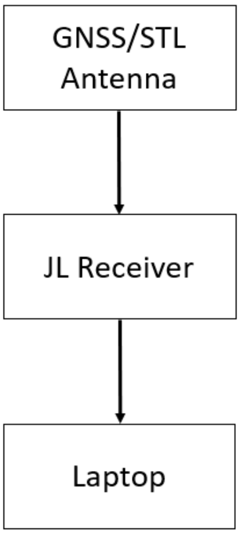

Figure 3.6: State Estimation Hardware Diagram with Internal TCXO

The second hardware configuration is targeted to assess the timing of the STL system against a GNSS-derived timebase. In this scenario, the SecureSync Time and Frequency Reference System disciplines the Stanford Research Systems FS725 Rubidium Frequency Standard, which feeds the JL STL-2600 receiver a 1-PPS and 10 MHz reference. Therefore, the STL system is not disciplining the oscillator, and the clock terms are relative to the GNSS-derived timebase. Theoretically, the bias and drift estimates are the offsets of the STL network from GPS time. This configuration is shown in Figure 3.7.

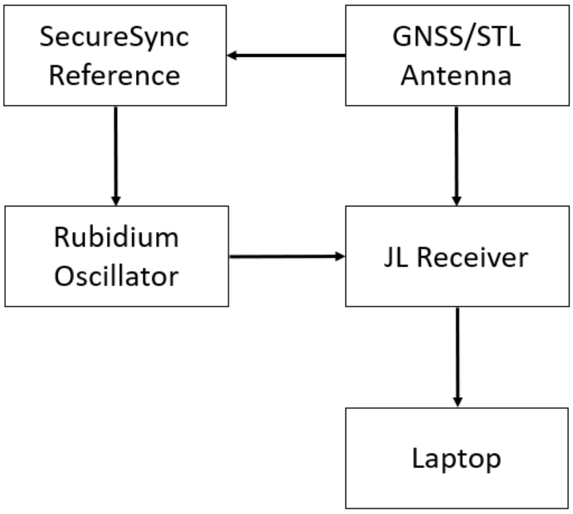

Figure 3.7: State Estimation Hardware Diagram with External Rubidium Oscillator

3.4 Timing State Estimation Algorithms

For timing state estimation, the measurements, models, and algorithms presented in Chapter 2 are used. In this experiment, three receiver conditions are considered. In the first test, the receiver is assumed to be at a precisely known, static position. In the second test, a static receiver position is thought to be known, but an incorrect position is provided to the filter. In both of these cases, only the receiver clock terms must be estimated, and the sensitivity of the solution to uncertainty in the receiver position is examined. Finally, in the third test, the position of a static receiver is unknown and must be estimated along with the clock terms, and the effect of the position estimation on the timing solution is examined.

3.4.1 EKF Timing Only Solution

For the first two scenarios, the ECEF position of the receiver is assumed to be known, leaving only the receiver clock bias and clock drift to be estimated. Therefore, a solution can be formed from the measurement models and estimation algorithms presented in Chapter 2. While a LS or WLS solution can be used, the receiver oscillator states are dynamic, rendering the EKF to be better suited for this application. The state vector for the solution is defined in

Equation (3.16),

$$\hat{\mathbf{x}} = \begin{bmatrix} \hat{b} \\ \hat{\dot{b}} \end{bmatrix} \tag{3.16}$$

where the receiver clock bias and frequency offset are estimated in units of seconds and seconds per second, respectively.

In this case, the system is propagated with a constant velocity dynamic model, which is shown in Equation (3.17) and Equation (3.18).

$$\hat{\mathbf{x}}_k = \mathbf{A}\hat{\mathbf{x}}_{k-1} + \mathbf{B}_w \varepsilon \tag{3.17}$$

$$\begin{bmatrix} \hat{b} \\ \hat{\dot{b}} \end{bmatrix}_k^- = \begin{bmatrix} 1 & \Delta t \\ 0 & 1 \end{bmatrix} \begin{bmatrix} \hat{b} \\ \hat{\dot{b}} \end{bmatrix}_{k-1}^+ + \begin{bmatrix} \varepsilon_b \\ \varepsilon_{\dot{b}} \end{bmatrix} \tag{3.18}$$

For the prediction phase, the receiver clock bias is calculated as a numerical integration, the receiver clock drift is assumed to be constant throughout the update period, and both states are modelled with zero mean, additive Gaussian noise. It should be noted that the JL STL-2600 receiver does not report measurements at fixed update intervals, so the state transition matrix is time-varying, and therefore must be updated for each epoch.

The estimate covariance matrix is calculated as a function of the state transition matrix, estimate covariance matrix, and process noise covariance matrix, which is shown in Equation (3.19).

$$\mathbf{P}_k^- = \mathbf{A}\mathbf{P}_{k-1}^+\mathbf{A}^T + \mathbf{Q} \tag{3.19}$$

The process noise covariance matrix is determined with the power spectral densities and coefficients from Table 3.1, which are extracted from the Allan variance analysis of both receiver clock types [67]. The general form of the process noise covariance matrix is shown in Equation (3.20).

$$\mathbf{Q} = \begin{bmatrix} S_f \Delta t + \frac{S_g \Delta t^3}{3} & \frac{S_g \Delta t^2}{2} \\ \frac{S_g \Delta t^2}{2} & S_g \Delta t \end{bmatrix} \tag{3.20}$$

For the measurement update, the filter is implemented at the tightly-coupled level, as the output measurements from the receiver module are pseudorange and Doppler shift. The pseudorange and pseudorange rate measurement models are shown in Equation (3.21) and Equation (3.22), respectively,

$$\hat{\rho} = r + c\hat{b} + \eta_{\rho} \tag{3.21}$$

$$\hat{\dot{\rho}} = \dot{r} + c\hat{\dot{b}} + \eta_{\dot{\rho}} \tag{3.22}$$

in which only the states in Equation (3.16) are estimated. From these models, the state-to-measurement mapping matrix can be obtained by calculating the Jacobian of the measurement model with respect to each state estimate and is shown in Equation (3.23).

$$\mathbf{H} = \begin{bmatrix} \frac{\partial\hat{\rho}}{\partial\hat{b}} & \frac{\partial\hat{\rho}}{\partial\hat{\dot{b}}} \\ \frac{\partial\hat{\dot{\rho}}}{\partial\hat{b}} & \frac{\partial\hat{\dot{\rho}}}{\partial\hat{\dot{b}}} \end{bmatrix} = \begin{bmatrix} c & 0 \\ 0 & c \end{bmatrix} \tag{3.23}$$

It may be noted that the mapping matrix is linear and time-invariant, and therefore not a function of the estimated states. Since the Jacobian matrix is constant, it does not need to be updated after initialization.

The mapping matrix and state covariance matrix can be combined with the measurement noise covariance matrix to obtain the Kalman gain matrix in Equation (3.24).

$$\mathbf{L} = \mathbf{P}_k^{-}\mathbf{H}^T(\mathbf{H}\mathbf{P}_k^{-}\mathbf{H}^T + \mathbf{R})^{-1} \tag{3.24}$$

The measurement noise of the pseudorange and pseudorange rate shown in Equation (3.25) are modeled as an exponential decay with respect to C/N_0.

$$\mathbf{R} = \begin{bmatrix} \sigma_{\rho}^2 & 0 \\ 0 & \sigma_{\dot{\rho}}^2 \end{bmatrix} \tag{3.25}$$

The C/N_0 values from the JL STL-2600 receiver range between 40 and 75 decibels (dB), resulting in a 1σ lower and upper bound of approximately 25 and 450 meters, respectively.

The mean noise ratio is typically approximately 60 dB, yielding a measurement error standard deviation of 84 meters.

From the Kalman gain matrix, the state vector and estimate covariance matrix can be obtained. The state vector is shown in Equation (3.26) and Equation (3.27),

$$\hat{\mathbf{x}}_k^+ = \hat{\mathbf{x}}_k^- + \mathbf{L}(\tilde{\mathbf{y}} - \hat{\mathbf{y}}) \tag{3.26}$$

$$\begin{bmatrix} \hat{b} \\ \hat{\dot{b}} \end{bmatrix}_k^+ = \begin{bmatrix} \hat{b} \\ \hat{\dot{b}} \end{bmatrix}_k^- + \mathbf{L}\left(\begin{bmatrix} \tilde{\rho} \\ \tilde{\dot{\rho}} \end{bmatrix} - \begin{bmatrix} \hat{\rho} \\ \hat{\dot{\rho}} \end{bmatrix} \right) \tag{3.27}$$

and the state covariance matrix is shown in Equation (3.28).

$$\mathbf{P}_k^+ = (\mathbf{I} - \mathbf{L}\mathbf{H})\mathbf{P}_k^- \tag{3.28}$$

Before implementing the filter, an observability analysis of the estimator should be conducted. Recalling Equation (2.31) and Equation (2.32), a system can be deemed observable if the rank of the observability matrix shown below is full.

$$\mathbf{O} = \begin{bmatrix} \mathbf{H} \\ \mathbf{HA} \\ \vdots \\ \mathbf{HA}^{n-1} \end{bmatrix} = \begin{bmatrix} \mathbf{H} \\ \mathbf{HA} \end{bmatrix}$$

Equation (3.29) defines the observability matrix,

$$\mathbf{O} = \begin{bmatrix} c & 0 \\ 0 & c \\ c & c\Delta t \\ 0 & c \end{bmatrix} \tag{3.29}$$

and Equation (3.30) shows the rank is full, resulting in an observable solution.

$$rank(\mathbf{O}) = 2 \tag{3.30}$$

3.4.2 WLS Position and Timing Solution

For the third test scenario, the position of the receiver is unknown, but the static assumption implies no velocity. Therefore, the state vector must be expanded to estimate a 3-D ECEF position, in addition to the clock terms. Equation (3.31) shows the new state vector,

$$\hat{\mathbf{x}} = \begin{bmatrix} \hat{\mathbf{p}} \\ \hat{b} \\ \hat{\dot{b}} \end{bmatrix} = \begin{bmatrix} \hat{x} \\ \hat{y} \\ \hat{z} \\ \hat{b} \\ \hat{\dot{b}} \end{bmatrix} \tag{3.31}$$

in which $\hat{\mathbf{p}} = [\hat{x},\ \hat{y},\ \hat{z}]^T$ contains the ECEF position coordinates of the receiver in meters, and $[\hat{b},\ \hat{\dot{b}}]^T$ are the receiver clock terms estimated in units of seconds and seconds per second, respectively.

Comparing the state vectors of the timing only and position and timing solutions, it is clear that the measurement models must be augmented. To account for the addition states, the pseudorange and pseudorange rate models should be updated as a function of the receiver position and receiver clock terms. The pseudorange model is shown in Equation (3.32).

$$\hat{\rho} = \hat{r} + c\hat{b} + \varepsilon_\rho$$

$$\hat{\rho} = ||\mathbf{p}_{SV} - \hat{\mathbf{p}}|| + c\hat{b} + \varepsilon_\rho \tag{3.32}$$

Under the static receiver assumption, the pseudorange rate model can be expressed as Equation (3.33) [71].

$$\hat{\dot{\rho}} = \hat{\dot{r}} + c\hat{\dot{b}} + \varepsilon_{\dot{\rho}}$$

$$\hat{\dot{\rho}} = \mathbf{v}_{SV} \cdot \frac{\mathbf{p}_{SV} - \hat{\mathbf{p}}}{||\mathbf{p}_{SV} - \hat{\mathbf{p}}||} + c\hat{\dot{b}} + \varepsilon_{\dot{\rho}} \tag{3.33}$$

Based on these models, the state-to-measurement mapping matrix must also be updated to account for the position states being added. Unlike the timing only model, the nonlinearities in the measurement models result in a Jacobian matrix that must be re-computed about the current state estimate for each iteration and update. The pseudorange and pseudorange rate mapping matrices are shown in Equation (3.34) and Equation (3.35), respectively,

$$\mathbf{H}_{\rho} = \begin{bmatrix} \frac{\partial\hat{\rho}}{\partial\hat{x}} & \frac{\partial\hat{\rho}}{\partial\hat{y}} & \frac{\partial\hat{\rho}}{\partial\hat{z}} & \frac{\partial\hat{\rho}}{\partial\hat{b}} & \frac{\partial\hat{\rho}}{\partial\hat{\dot{b}}} \end{bmatrix}$$

$$\mathbf{H}_{\rho} = \begin{bmatrix} -\frac{x_{SV}-\hat{x}}{||\mathbf{p}_{SV}-\hat{\mathbf{p}}||} & -\frac{y_{SV}-\hat{y}}{||\mathbf{p}_{SV}-\hat{\mathbf{p}}||} & -\frac{z_{SV}-\hat{z}}{||\mathbf{p}_{SV}-\hat{\mathbf{p}}||} & c & 0 \end{bmatrix} \tag{3.34}$$

$$\mathbf{H}_{\hat{\dot{\rho}}} = \begin{bmatrix} \frac{\partial\hat{\dot{\rho}}}{\partial\hat{x}} & \frac{\partial\hat{\dot{\rho}}}{\partial\hat{y}} & \frac{\partial\hat{\dot{\rho}}}{\partial\hat{z}} & \frac{\partial\hat{\dot{\rho}}}{\partial\hat{b}} & \frac{\partial\hat{\dot{\rho}}}{\partial\hat{\dot{b}}} \end{bmatrix}$$

$$\mathbf{H}_{\hat{\dot{\rho}}} = \begin{bmatrix} \frac{\mathbf{p}_{SV}-\hat{\mathbf{p}}}{||\mathbf{p}_{SV}-\hat{\mathbf{p}}||} \times (\frac{\mathbf{p}_{SV}-\hat{\mathbf{p}}}{||\mathbf{p}_{SV}-\hat{\mathbf{p}}||} \times \frac{\mathbf{v}_{SV}}{||\mathbf{p}_{SV}-\hat{\mathbf{p}}||}) & 0 & c \end{bmatrix} \tag{3.35}$$

and the combined solution is shown in Equation (3.36).

$$\mathbf{H} = \begin{bmatrix} \mathbf{H}_{\rho} \\ \\ \mathbf{H}_{\hat{\dot{\rho}}} \end{bmatrix} = \begin{bmatrix} \frac{\partial\hat{\rho}}{\partial\hat{x}} & \frac{\partial\hat{\rho}}{\partial\hat{y}} & \frac{\partial\hat{\rho}}{\partial\hat{z}} & \frac{\partial\hat{\rho}}{\partial\hat{b}} & \frac{\partial\hat{\rho}}{\partial\hat{\dot{b}}} \\ \frac{\partial\hat{\dot{\rho}}}{\partial\hat{x}} & \frac{\partial\hat{\dot{\rho}}}{\partial\hat{y}} & \frac{\partial\hat{\dot{\rho}}}{\partial\hat{z}} & \frac{\partial\hat{\dot{\rho}}}{\partial\hat{b}} & \frac{\partial\hat{\dot{\rho}}}{\partial\hat{\dot{b}}} \end{bmatrix}$$

$$\mathbf{H} = \begin{bmatrix} -\frac{\mathbf{p}_{SV}-\hat{\mathbf{p}}}{||\mathbf{p}_{SV}-\hat{\mathbf{p}}||} & c & 0 \\ \frac{\mathbf{p}_{SV}-\hat{\mathbf{p}}}{||\mathbf{p}_{SV}-\hat{\mathbf{p}}||} \times (\frac{\mathbf{p}_{SV}-\hat{\mathbf{p}}}{||\mathbf{p}_{SV}-\hat{\mathbf{p}}||} \times \frac{\mathbf{v}_{SV}}{||\mathbf{p}_{SV}-\hat{\mathbf{p}}||}) & 0 & c \end{bmatrix} \tag{3.36}$$

From $\frac{\mathbf{v}_{SV}}{||\mathbf{p}_{SV}-\hat{\mathbf{p}}||}$ in Equation (3.35) and Equation (3.36), it is apparent that the reduced altitude results in greater geometric sensitivity, and therefore, when compared to GPS, improves the observability and performance of the Doppler-based position solution.

While not incorporated in the WLS solution, a state transition matrix is required for an observability analysis, which is shown in Equation (3.37).

$$\mathbf{A} = \begin{bmatrix} 1 & 0 & 0 & 0 & 0 \\ 0 & 1 & 0 & 0 & 0 \\ 0 & 0 & 1 & 0 & 0 \\ 0 & 0 & 0 & 1 & \Delta t \\ 0 & 0 & 0 & 0 & 1 \end{bmatrix} \tag{3.37}$$

From the state transition and state-to-measurement mapping matrices, the rank of the observability matrix is not full from a single measurement epoch. To account for this issue, measurements are batched in time, augmenting the mapping matrix **H** to:

$$\mathbf{H} = \begin{bmatrix} -\frac{\mathbf{p}^1_{SV}-\hat{\mathbf{p}}}{||\mathbf{p}^1_{SV}-\hat{\mathbf{p}}||} & c & 0 \\ \frac{\mathbf{p}^1_{SV}-\hat{\mathbf{p}}}{||\mathbf{p}^1_{SV}-\hat{\mathbf{p}}||} \times (\frac{\mathbf{p}^1_{SV}-\hat{\mathbf{p}}}{||\mathbf{p}^1_{SV}-\hat{\mathbf{p}}||} \times \frac{\mathbf{v}^1_{SV}}{||\mathbf{p}^1_{SV}-\hat{\mathbf{p}}||}) & 0 & c \\ -\frac{\mathbf{p}^2_{SV}-\hat{\mathbf{p}}}{||\mathbf{p}^2_{SV}-\hat{\mathbf{p}}||} & c & 0 \\ \frac{\mathbf{p}^2_{SV}-\hat{\mathbf{p}}}{||\mathbf{p}^2_{SV}-\hat{\mathbf{p}}||} \times (\frac{\mathbf{p}^2_{SV}-\hat{\mathbf{p}}}{||\mathbf{p}^2_{SV}-\hat{\mathbf{p}}||} \times \frac{\mathbf{v}^2_{SV}}{||\mathbf{p}^2_{SV}-\hat{\mathbf{p}}||}) & 0 & c \\ \vdots & \vdots & \vdots \\ -\frac{\mathbf{p}^j_{SV}-\hat{\mathbf{p}}}{||\mathbf{p}^j_{SV}-\hat{\mathbf{p}}||} & c & 0 \\ \frac{\mathbf{p}^j_{SV}-\hat{\mathbf{p}}}{||\mathbf{p}^j_{SV}-\hat{\mathbf{p}}||} \times (\frac{\mathbf{p}^j_{SV}-\hat{\mathbf{p}}}{||\mathbf{p}^j_{SV}-\hat{\mathbf{p}}||} \times \frac{\mathbf{v}^j_{SV}}{||\mathbf{p}^j_{SV}-\hat{\mathbf{p}}||}) & 0 & c \end{bmatrix} \tag{3.38}$$

and the measurement vector to:

$$\tilde{\mathbf{y}} = \begin{bmatrix} \tilde{\rho}^1 \\ \tilde{\dot{\rho}}^1 \\ \tilde{\rho}^2 \\ \tilde{\dot{\rho}}^2 \\ \vdots \\ \tilde{\rho}^j \\ \tilde{\dot{\rho}}^j \end{bmatrix}, \tag{3.39}$$

where each *j*-th satellite burst populates a row for both the pseudorange and pseudorange rate.

The measurement error vector ($\delta \mathbf{y}$) is computed as the difference between the measured pseudorange and rate and the estimates from the models in Equation (3.32) and Equation (3.33) and is shown in Equation (3.40).

$$\delta \mathbf{y} = \tilde{\mathbf{y}} - \hat{\mathbf{y}} = \begin{bmatrix} \tilde{\rho}^1 - \hat{\rho}^1 \\ \tilde{\dot{\rho}}^1 - \hat{\dot{\rho}}^1 \\ \tilde{\rho}^2 - \hat{\rho}^2 \\ \tilde{\dot{\rho}}^2 - \hat{\dot{\rho}}^2 \\ \vdots \\ \tilde{\rho}^j - \hat{\rho}^j \\ \tilde{\dot{\rho}}^j - \hat{\dot{\rho}}^j \end{bmatrix} \tag{3.40}$$

The results of this study are calculated with batch windows of 5 minutes, which provides the estimator with enough measurements to observe the solution. Additionally, the extended window allows for measurements from multiple satellites to be processed and improves the satellite geometry from a single, 2-D plane to a 3-D space.

Similarly to the measurement noise covariance matrix in Equation (3.25), the C/N_0 values reported by the JL STL-2600 receiver were used to populate **W**. As the measurement noise is a metric of the uncertainty of the system, the inverse of covariance describes of the certainty. Therefore, the weighting matrix **W** is calculated as the inverse of the process noise covariance matrix, which is shown in Equation (3.41).

$$\mathbf{W} = \mathbf{R}^{-1} \tag{3.41}$$

3.4.3 Filter Initialization

In both estimation frameworks, an initial value for the state vector and covariance matrix must be provided. A popular approach is to input a vector of zeros for the state vector and represent the great uncertainty of the initial conditions with large values in the state covariance matrix. While this method can be used, it may cause the solution to converge to an incorrect solution space or diverge entirely. To mitigate this risk, both filters were provided a 10-minute initialization period, in which the receiver position was assumed to be known. A LS solution was used to estimate the receiver clock bias and drift, and the state estimates were fed into the EKF and WLS algorithms as the initial conditions. For the initial state covariance matrix, the values were conservatively set to bound the uncertainty of the LS solution and allow the filters to converge.

3.4.4 Error Rejection

While both the EKF and WLS algorithms are designed to account for measurement uncertainty, an additional step to remove outlier measurements must be done. Particularly for the WLS solution, outlier measurements can be detrimental to the estimator, as excessive errors propagate into dramatic state estimate errors, thus degrading performance. To mitigate this risk, state estimates outside of a pre-defined threshold were rejected. For timing applications, the most obvious error detection metric is the receiver clock drift. Large values of drift often correlate to errant measurements, as the JL STL-2600 receiver module is designed to steer the local oscillator with small frequency adjustments. For this experiment, a threshold of 10 nanoseconds per seconds is used to detect estimate errors, which is executed with the following logic.

```
if abs(rcvrClockDrift) > 10e-9
    errorDetectedBool = true;
else
    errorDetectedBool = false;
end
```

3.5 On-Board TCXO Results

For the first configuration of this experiment, approximately 24 hours of live-sky data was collected with the off-the-shelf JL STL-2600 receiver module operating with an on-board TCXO. To coherently display the findings of this study, the EKF with knowledge of the true receiver position and WLS outputs are presented together. The error rejection technique is tested in both solutions, and the results and statistics are compared to assess the uncertainty introduced by estimating the receiver position in addition to the clock states. Next, a sensitivity analysis is presented to gauge the effect of error in the known receiver position for the EKF implementation. This process is repeated for the second receiver configuration, and the improvements of integrating a higher-grade oscillator are analyzed.

Prior to integrating error rejection in the WLS solution, both filters were implemented to post-process live-sky data collected with the Jackson Labs STL-2600 receiver for approximately 24 hours. The state estimation results of the receiver clock bias and drift for the EKF and WLS are shown in Figure 3.8, and the estimate standard deviations are shown in Figure 3.9. From these plots, three conclusions can already be drawn. First, the scaling on the receiver clock bias renders the results difficult to interpret. Recalling the raw pseudorange plot in Figure 3.2, the values of the range measurements are significantly greater than expected, implying an inherent, intentional timing offset in the receiver module. For the remainder of this study, timing results are presented and analyzed with the initial offset removed. Second, large measurement errors dramatically degrade the performance of the WLS filter. In the EKF, errant measurements lead to a spike in the state estimate, which requires additional time to converge and results in nonsensical state estimates. For this reason, the error detection algorithm is already integrated into the filter. For the WLS, the severity of this effect is likely due to the lack of a time update to reject outlier measurements, and therefore calls for an external rejection technique to be employed. Third, both filters do converge, which serves as a validation of the observability analysis previously conducted.

Before analyzing the estimates, Figure 3.10 shows the convergence of the state covariance after the 10-minute initialization period. From the plot, it can be observed that both filters converge fairly quickly. The timing only EKF converges to within 12 nanoseconds in approximately 2 minutes, and the WLS solution converges within the first estimate after the initial batch of 10 minutes. After 2 minutes, the EKF continues to converge, and complete convergence is assumed after 4 hours. The post-settling mean receiver clock bias uncertainty for the EKF and WLS solutions are 7.4 and 8.7 nanoseconds, respectively.

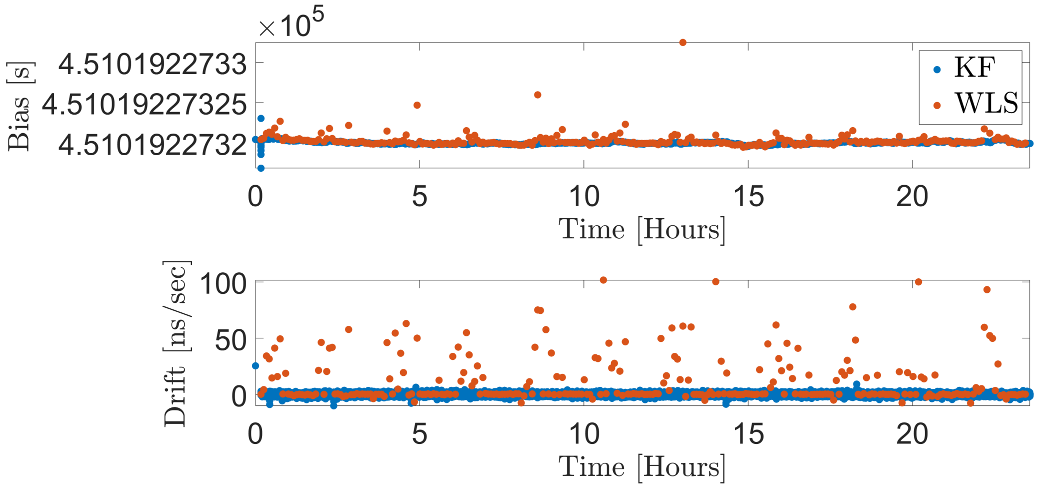

Figure 3.8: Timing State Estimates with Internal TCXO

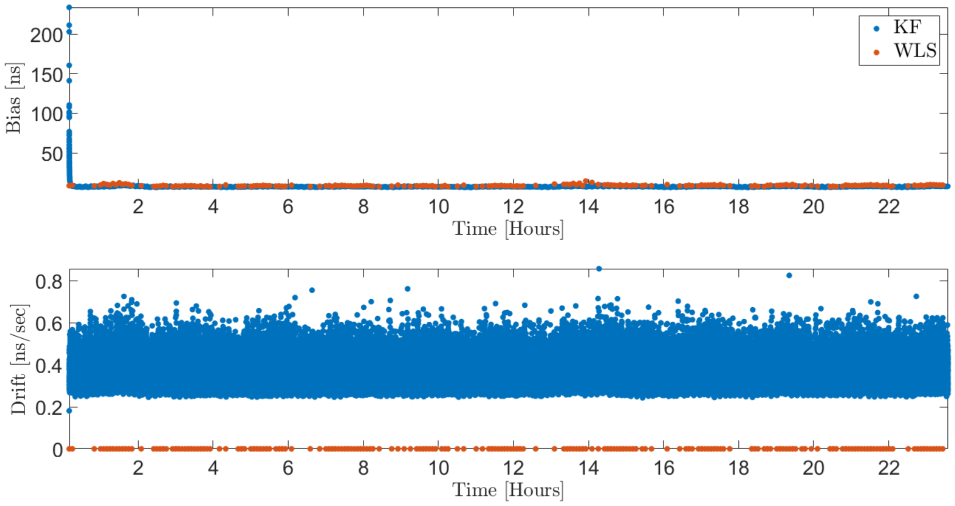

Figure 3.9: State Estimate 1σ Deviation with Internal TCXO

The error rejection technique used in this work is in the state domain, which was described previously in Section 3.4.4. With this method, the filters operate as normal, but update epochs in which the receiver clock drift estimate is greater than the pre-defined threshold of 10 nanoseconds per second are rejected, and the previous state vector is used. While this technique is effective for removing errant estimates, the WLS is updated as frequently as the batch window. In this case, each rejected estimate results in a 5-minute outage, which can be detrimental to systems requiring frequent timing updates. In practice, a sliding batch window should be used,

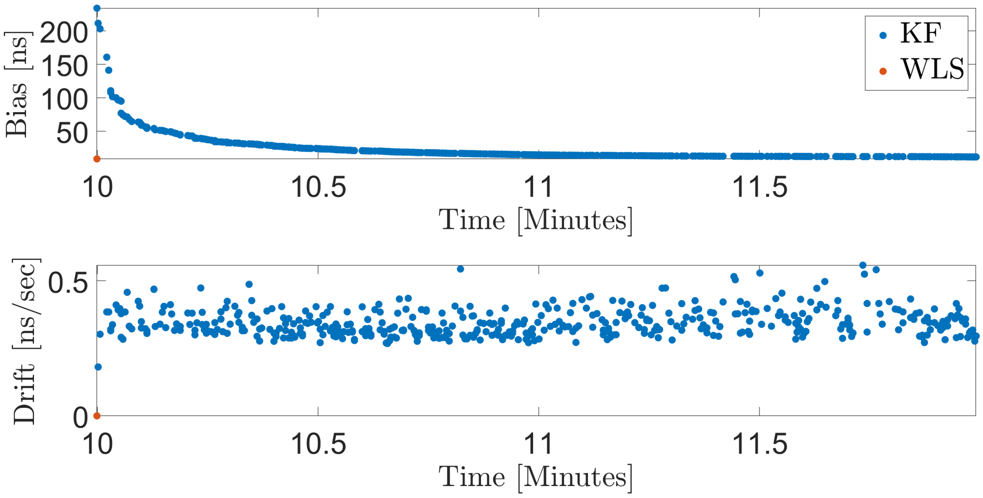

Figure 3.10: Pre-Convergence State Estimate 1σ Deviation with Internal TCXO

which adds a new measurement to the solution and drops the oldest. However, the implementation without the sliding window provides insight into the number of satellites in view for each update and the number of errant estimates rejected. Figure 3.11 shows the number of satellites in view for each measurement update of the WLS solution, and blank entries denote a rejected solution.

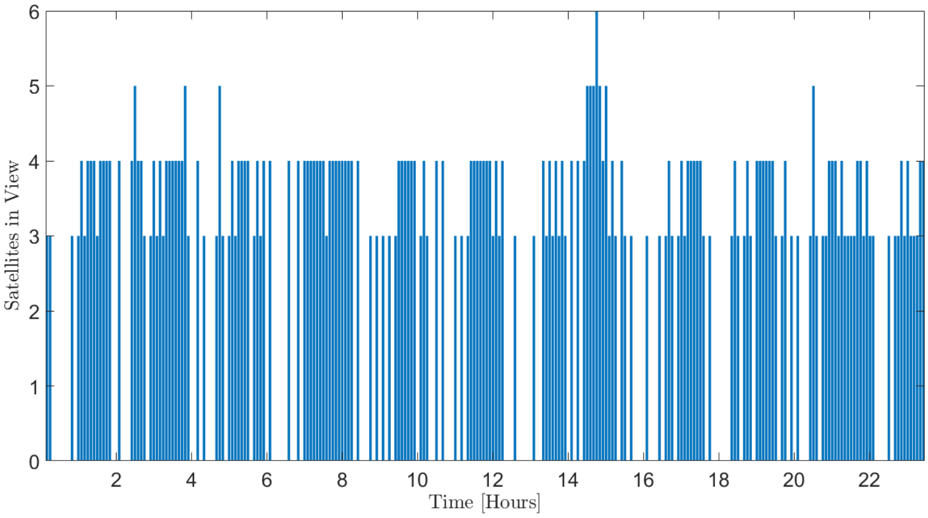

Figure 3.11: WLS Satellite Visibility with Internal TCXO

For this collection period, measurements from at least 3 Iridium satellites were received during each batch window, which is sufficient to effectively estimate the receiver position and clock states. However, only 67% of the estimates are within the clock drift threshold, which will be compared in the next section. Finally, the post-convergence receiver clock states are shown in Figure 3.12, and the estimate statistics are shown in Table 3.2. It should be noted that the mean bias is not necessarily the mean of the clock error, but rather the mean difference between the estimates and the initial value that was removed. These values are effectively the realization of thermal noise on the timing solution.

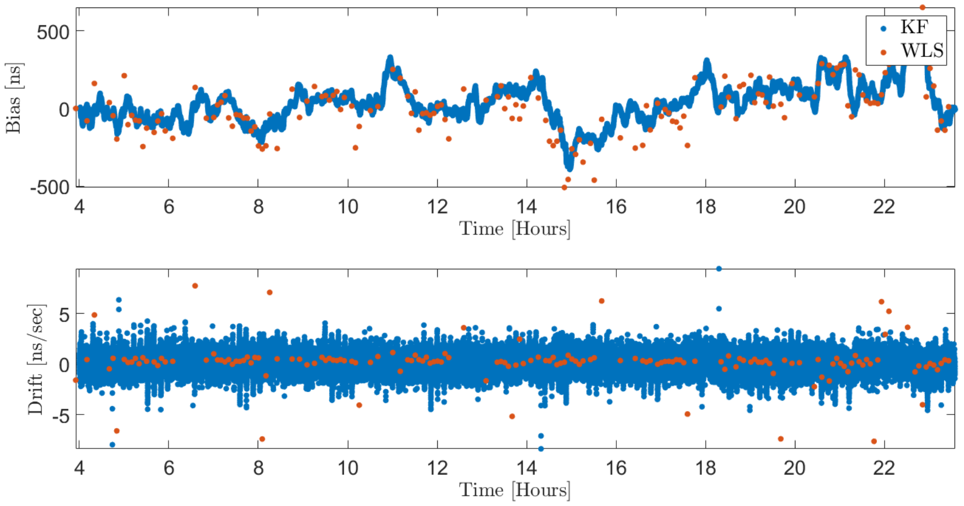

Figure 3.12: Post-Convergence Timing State Estimates with Internal TCXO

Table 3.2: Post-Convergence Timing State Estimate Statistics with Internal TCXO

	EKF: Timing Only	**WLS: Position and Timing**
Bias Mean	38.26 ns	1.05 ns
Bias Standard Deviation	133.07 ns	177.78 ns
Drift Mean	0.046 ns/s	0.18 ns/s
Drift Standard Deviation	0.69 ns/s	1.98 ns/s

3.6 External Rubidium Oscillator Results

For the second configuration of this experiment, an external, GNSS-disciplined rubidium reference oscillator was integrated into the JL STL-2600 receiver module. The results for this configuration are presented in the same manner as the previous section. First, both filters were executed with live-sky data collected with the second hardware configuration described in

Section 3.3, and the state estimates and covariances are shown in Figure 3.13 and Figure 3.14, respectively. Again, it is clear that both filters converge.

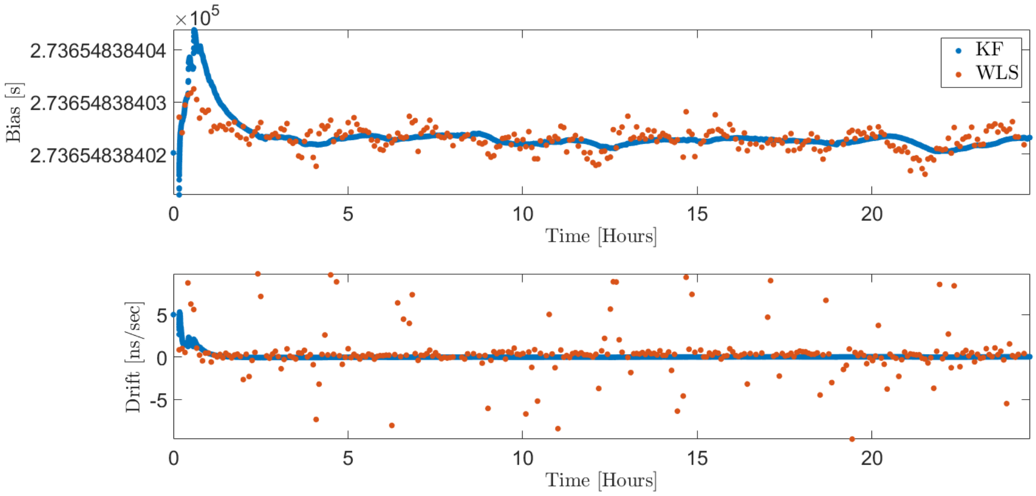

Figure 3.13: Timing State Estimates with External Rubidium Oscillator

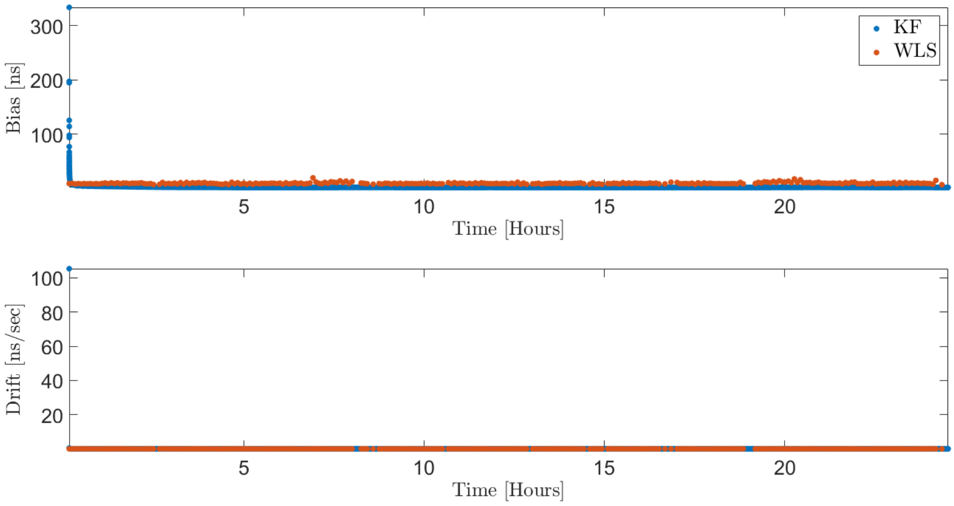

Figure 3.14: State Estimate 1σ Deviation with External Rubidium Oscillator

The covariance convergence of the timing solutions are shown in Figure 3.15. Inspecting the curve, it is first apparent that the EKF converges slower with this configuration than the previous, which is to be expected based on the the lower process to measurement noise ratio. The timing only solution converges to 10 nanoseconds in approximately 2.5 minutes, and the mean, post-settling EKF and WLS 1σ deviations are 4.16 and 9.45 nanoseconds, respectively.

Considering the rubidium estimator converges slower than the TCXO, convergence is assumed after 6 hours.

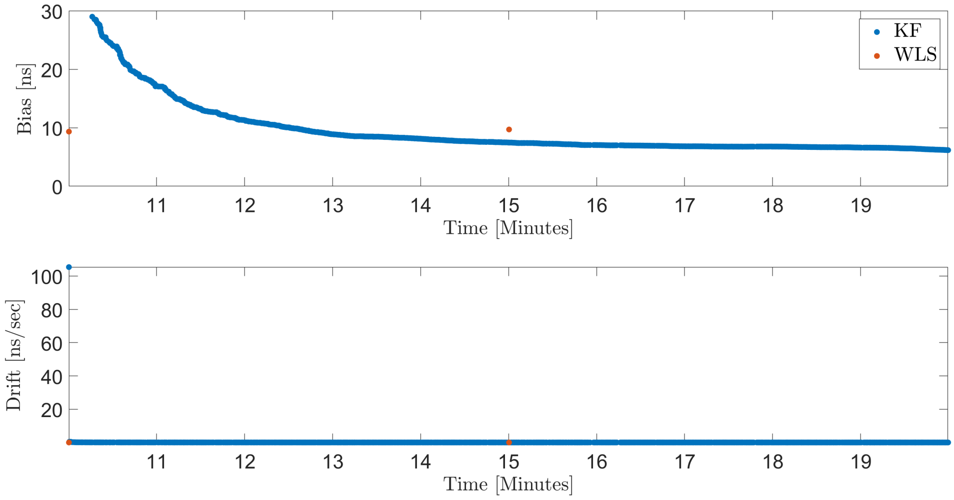

Figure 3.15: Pre-Convergence State Estimate 1σ Deviation with External Rubidium Oscillator

The error rejection method was employed on the timing solution with an incorporated external rubidium oscillator. Again, a 5-minute batch window was used for the WLS estimator, providing an observable solution and measurements from multiple satellites. Figure 3.16 shows the satellite visibility for each batch window, where 95% of the estimates were within the receiver clock drift threshold. Compared to the 67% validity in the previous section, an immediate improvement can be noticed. Additionally, this data set also shows at least 3 satellites in view for each update, and as many as 7 are measured. Generally, the number of visible satellites directly correlate to observability for position estimation.

Finally, the post-convergence state estimates are shown in Figure 3.17, and the estimate statistics are given in Table 3.3. Comparing Table 3.2 and Table 3.3, the timing only solution is dramatically improved when the rubidium oscillator is utilized. Particularly, the bias standard deviation and drift statistics are significantly reduced. For the WLS implementation, the results are comparable, but the timing accuracy improvement is not as clear. A likely explanation for the lack of apparent improvement is the receiver oscillator stability is not directly incorporated into the estimation algorithm through the prediction phase, resulting in the filter relying entirely on the satellite measurements to update the states. Alternatively, external conditions, such

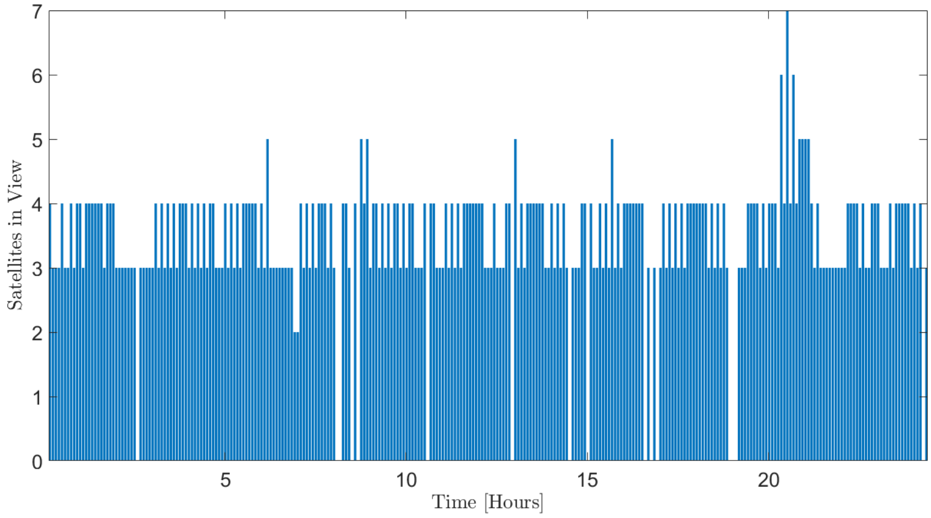

Figure 3.16: WLS Satellite Visibility with External Rubidium Oscillator

as atmosphere, weather, and inherent error in the STL network, could negatively impact the accuracy of the solution.

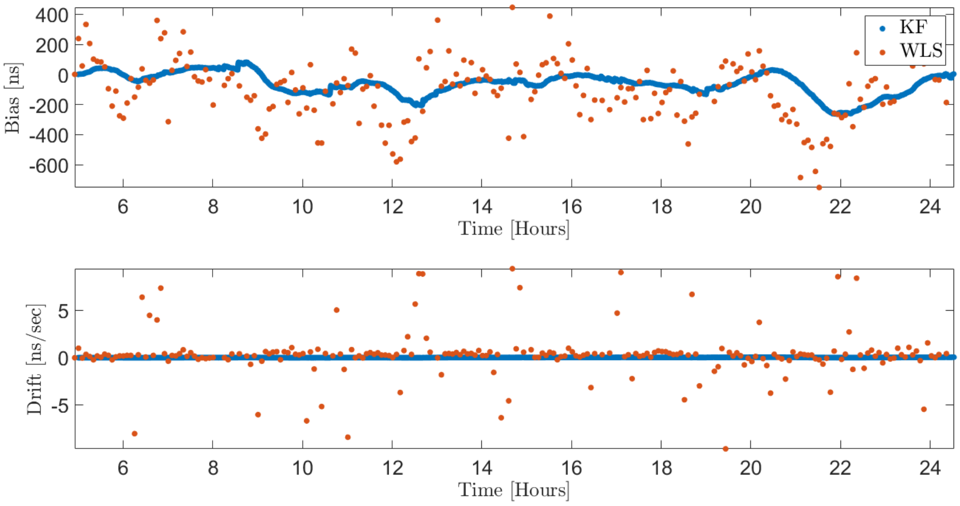

Figure 3.17: Post-Convergence Timing State Estimates with External Rubidium Oscillator

3.7 Effect of Receiver Position Error on Timing Performance

In the previous sections, both configurations were tested to assess how estimating the receiver position affects the timing performance of the receiver. This section assesses the impact of feeding an incorrect receiver position value to the EKF. To gauge this influence, the EKF

Table 3.3: Post-Convergence Timing State Estimate Statistics with External Rubidium Oscillator

	EKF: Timing Only	**WLS: Position and Timing**
Bias Mean	-62.43 ns	-100.03 ns
Bias Standard Deviation	73.36 ns	205.31 ns
Drift Mean	-0.0032 ns/s	0.29 ns/s
Drift Standard Deviation	0.01 ns/s	2.49 ns/s

architecture presented in Section 3.4 is tested with several magnitudes of position error, and the results are compared. Total position errors of 100, 500, and 1000 kilometers are provided to the filter with the same data set used in the previous sections, and a plot of the tested positions are shown in Figure 3.18.

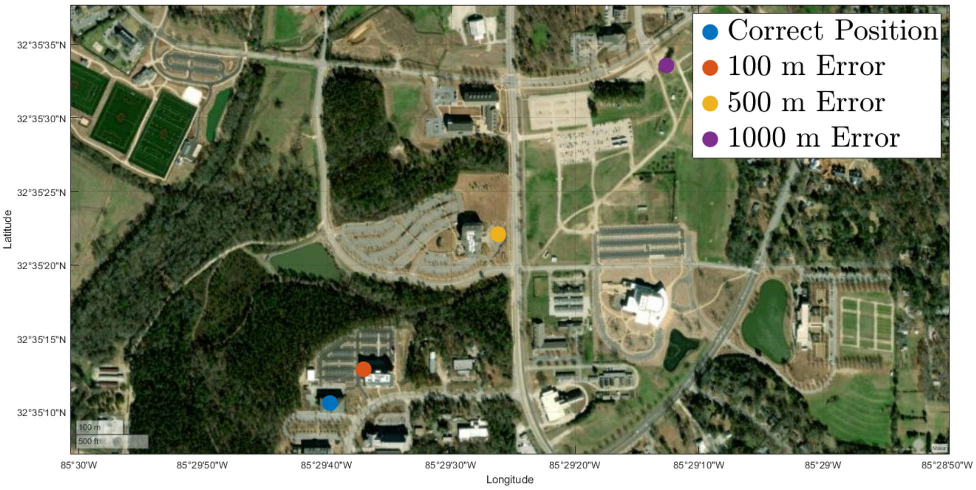

Figure 3.18: EKF Receiver Position Inputs

The TCXO-driven EKF receiver clock bias and drift estimates for each case are presented in Figure 3.19 and Figure 3.20, respectively. From the plots, it is clear that as the clock state estimates differ from truth as the receiver position error increases. Additionally, in the receiver clock drift plot, it is apparent that the error in position results in a non-zero mean frequency offset, resulting in incorrect timing corrections being communicated to the oscillator.

To quantify the effects of receiver position error on the timing solution, the state estimates were synchronized in time, and the difference between each scenario and *truth* was calculated. It should be noted that the *true* states were also estimated with measurement uncertainty, so the

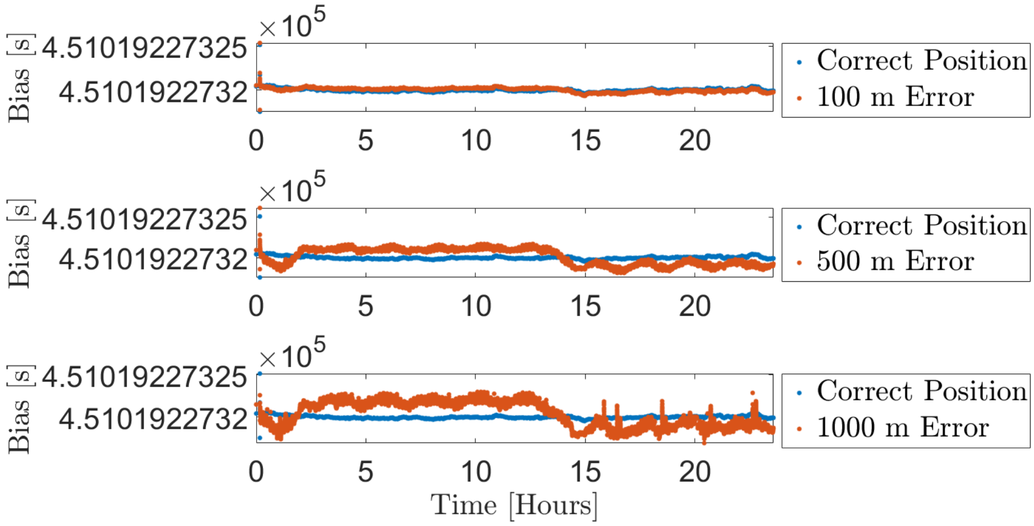

Figure 3.19: Receiver Clock Bias with Position Error (Internal TCXO)

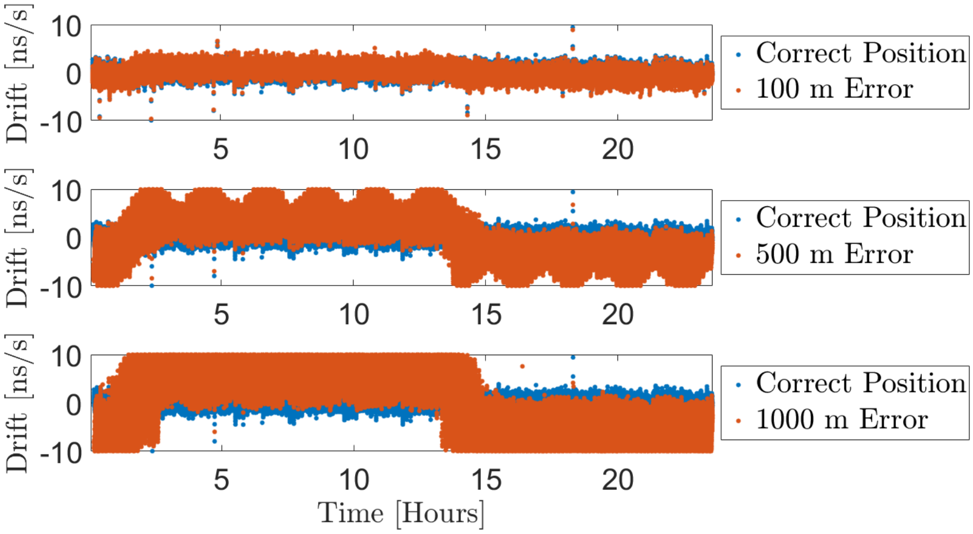

Figure 3.20: Receiver Clock Drift with Position Error (Internal TCXO)

results presented cannot be considered absolute error. The receiver clock bias and drift estimate errors are shown in Figure 3.21 and Figure 3.22, respectively, and the results are summarized in Table 3.4.

For comparison, the same methodology was executed for the data set collected with the rubidium clock input. The receiver clock terms are shown in Figure 3.23 and Figure 3.24. Comparing these plots to the previous configuration, the effects of position errors are significantly less dramatic, but they still result in error and oscillation in the timing solution.

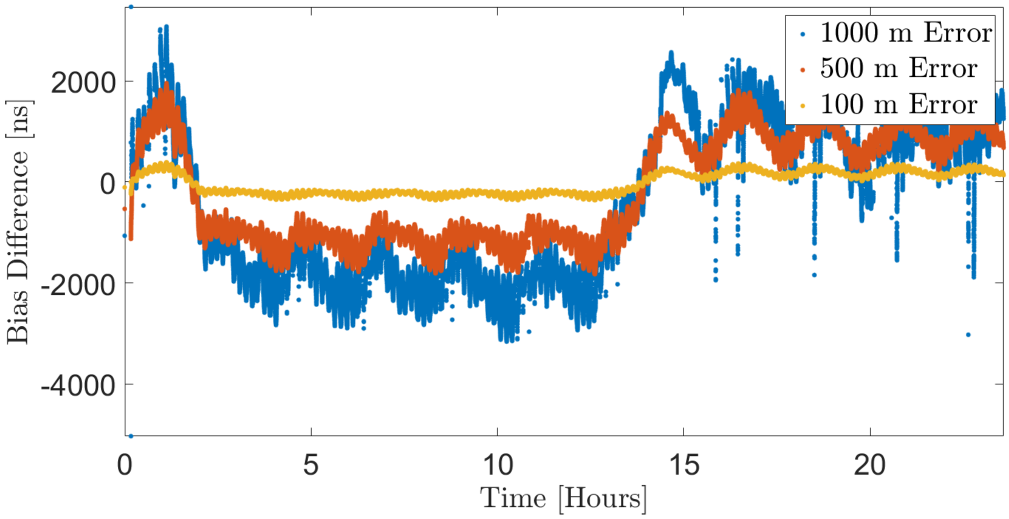

Figure 3.21: Receiver Clock Bias Error (Internal TCXO)

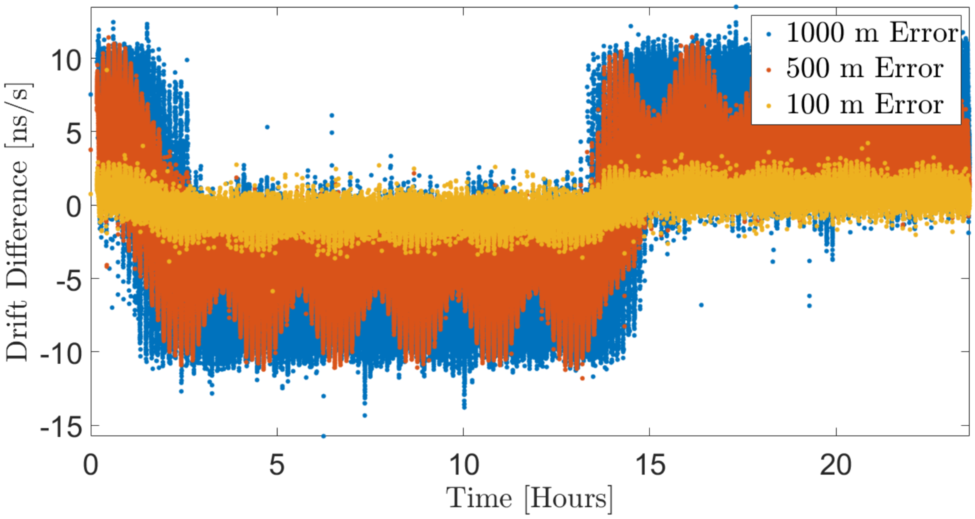

Figure 3.22: Receiver Clock Drift Error (Internal TCXO)

Table 3.4: Timing State Estimate Error (Internal TCXO)

	100 m Error	**500 m Error**	**1000 m Error**
Bias Mean	-28.19 ns	-124.04 ns	-413.80 ns
Bias Standard Deviation	221.36 ns	1068.31 ns	1519.71 ns
Drift Mean	-0.04 ns/s	-0.17 ns/s	-0.47 ns/s
Drift Standard Deviation	0.95 ns/s	4.46 ns/s	5.61 ns/s

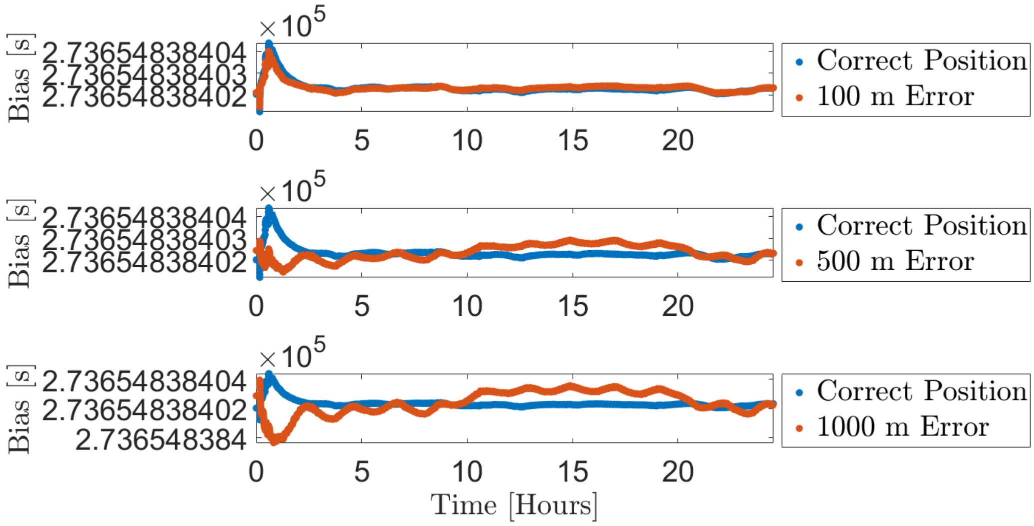

Figure 3.23: Receiver Clock Bias with Position Error (External Rubidium Oscillator)

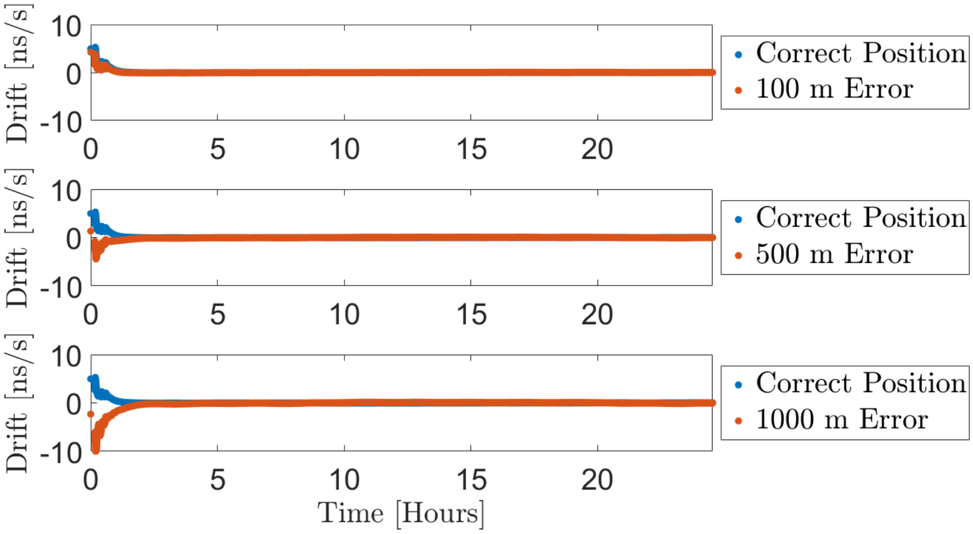

Figure 3.24: Receiver Clock Drift with Position Error (External Rubidium Oscillator)

Similarly to the first configuration, the timing state error statistics were calculated. The receiver clock bias error is shown in Figure 3.25, and the drift errors are shown in Figure 3.26. The results are summarized in Table 3.5.

Comparing the error plots to the previous configuration, it is clear that the improved receiver clock reduces the oscillations in the timing solution. Additionally, the receiver frequency offset is dramatically reduced. Inspecting the error statistic tables, the rubidium-disciplined

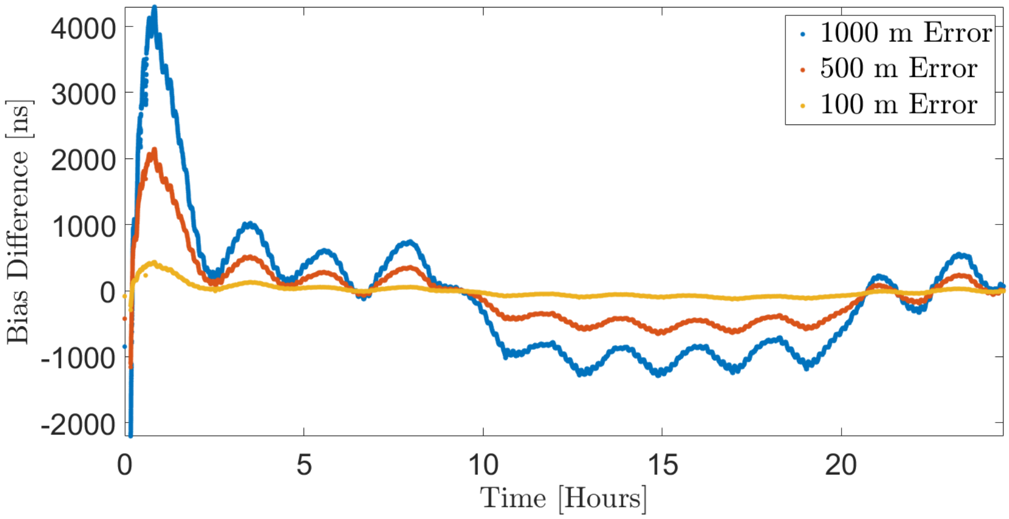

Figure 3.25: Receiver Clock Bias Error (External Rubidium Oscillator)

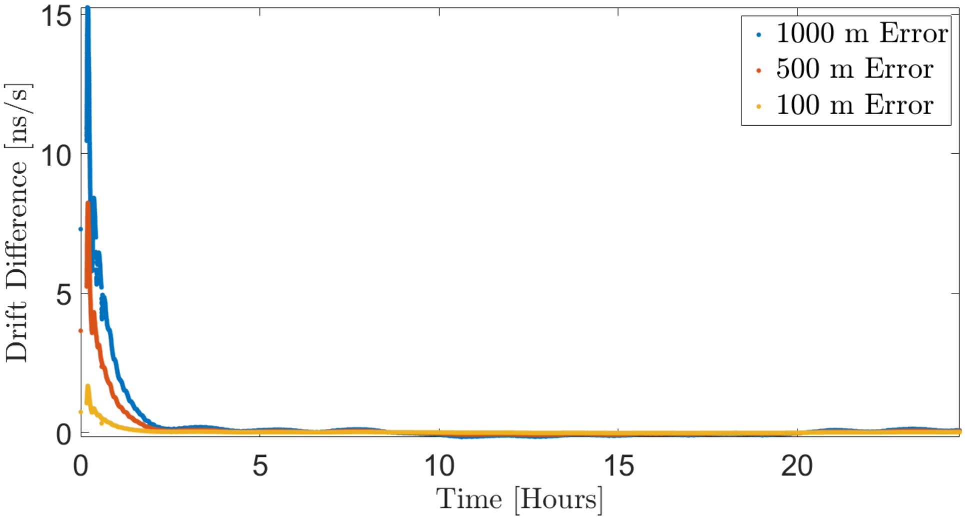

Figure 3.26: Receiver Clock Drift Error (External Rubidium Oscillator)

Table 3.5: Timing State Estimate Error (External Rubidium Oscillator)

	100 m Error	**500 m Error**	**1000 m Error**
Bias Mean	-5.34 ns	-36.45 ns	-74.16 ns
Bias Standard Deviation	102.77 ns	531.29 ns	1056.94 ns
Drift Mean	0.02 ns/s	0.12 ns/s	0.24 ns/s
Drift Standard Deviation	0.13 ns/s	0.67 ns/s	1.19 ns/s

configuration performs better in every category. Specifically, the error standard deviations verify the oscillations have been reduced, and the reduction in the drift terms indicate a higher-fidelity solution.

3.8 Conclusions

In this study, a total of 48 hours of live-sky, STL data was collected and processed. In the known and unknown receiver position conditions, the STL timing solution proved to be of sub-microsecond-level precision and highly-stable. However, it was demonstrated that accurate knowledge of the receiver position improved the timing accuracy and deviation. In the sensitivity analysis of error in the receiver position, timing error increases with position error, but the effects are significantly reduced when a high-fidelity oscillator is integrated into the circuit. Configuration 1 demonstrated that the STL system successfully disciplines the on-board TCXO clock to a high degree. Minor variations in the receiver clock states are expected, but the timing errors are bounded for both receiver position scenarios. Configuration 2 demonstrated the advantage of integrating a local, atomic oscillator into the receiver hardware, particularly in the timing only solution. In the position and timing estimation, the results are comparable, but the improvements are less apparent. A potential explanation for this discrepancy is the oscillator stability is not factored into the estimation algorithm. Additionally, the next chapter demonstrates the variability in the timing of the STL system, in which the capabilities are shown to vary slightly day-to-day.

Chapter 4

Receiver Time Interval Study

4.1 Introduction and Theory

In the previous chapter, the internal observables from the JL STL-2600 module were extracted and used to estimate the receiver clock bias and drift, which are critical to maintaining nanosecond-level timing accuracy. Aside from keeping accurate GPS time, satellite navigation also provides frequency references, which are used for network and sensor synchronization. As previously described in Chapter 1, the two primary frequency signals of receiver modules are a 1 Hz, or 1-PPS, and 10 MHz voltage outputs. For the purposes of this thesis, the 10 MHz reference will be used as an internal reference in the receiver hardware, and the 1-PPS output will be analyzed to quantify the timing accuracy of the receiver, which is common procedure in the prior art [32–34].

The 1-PPS voltage output from the JL STL-2600 receiver is a 3.3-V square wave, and is generated at each integer GPS second. This experiment aims to compare the actual timing outputs between the JL receiver module and a GNSS-disciplined frequency reference system through a time difference measurement. This difference is calculated as the time interval between the 50% point of the rising edge of the reference and tested signals, which is illustrated in Figure 4.1. The primary objectives of this experiment are as follows.

- Test the 1-PPS timing capabilities of the TCXO-disciplined JL STL-2600 receiver module
- Integrate an external, rubidium oscillator and compare results between receiver hardware configurations

- Assess error statistics and obtain low-confidence error bounds for mean, standard deviation, and maximum error

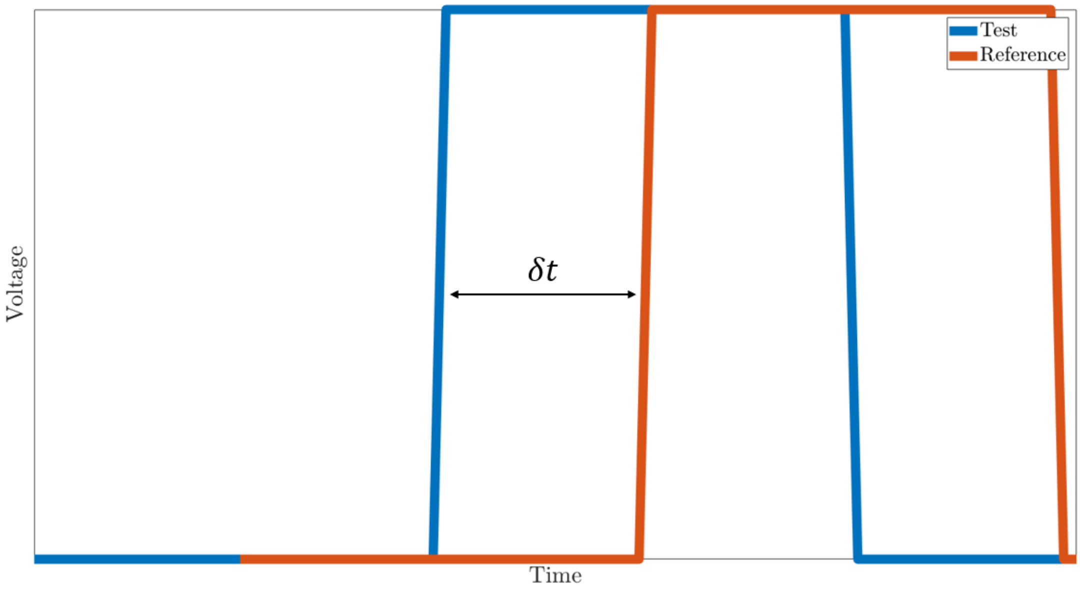

Figure 4.1: 1-PPS Time Interval Example

4.2 Hardware Configurations

From the first experiment, much of the data collection equipment is the same. In this study, two JL STL-2600 receivers are used simultaneously, and the reference signal is obtained from the SecureSync Time and Frequency Reference System. The STL receivers are tested with both the on-board, TCXO and external, rubidium oscillator, and both are compared to the GNSS-disciplined reference. The 1-PPS outputs from each of the three receivers are fed into a Tektronix MDO 3024 oscilloscope, which samples at 2.5 gigasamples per second, resulting in 400 picoseconds of time interval resolution. The oscilloscope is connected to the HP data collection laptop, which utilizes the open-source, TekScope Utility to communicate with the device, configure settings, and log the time delay measurements at 10-second intervals to a CSV file format. Once collection was completed, the CSV files were imported, processed, and analyzed in MATLAB.

The results of this study were obtained from three, 24-hour collection periods. In each of the tests, the true receiver position was provided to the STL receivers, and the GPS capabilities were disabled. The receivers were also provided sufficient time (approximately 1 hour) to acquire the STL signal and converge to a solution. The first two collections utilize the factory, JL STL-2600 receiver module and compare the timing accuracy variation between two calendar days. The 1-PPS output pins were fed directly to the oscilloscope, which calculated time delay measurements between each receiver and the reference signal. The hardware diagram is shown in Figure 4.2.

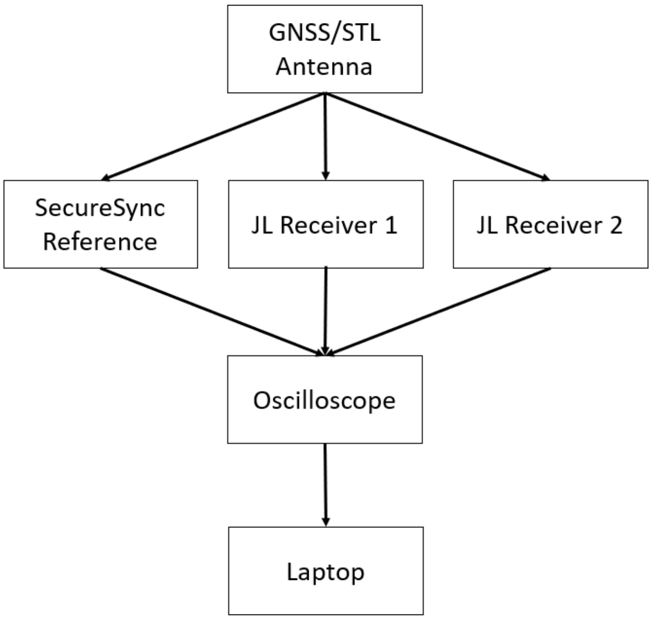

Figure 4.2: Time Interval Hardware Diagram with TCXO

For the third collection period, a similar setup was configured. However, an external, rubidium oscillator was integrated into one of the JL STL-2600 receivers. The receiver was provided a 1-PPS and 10 MHz reference from the oscillator, and the oscillator was fed the 1-PPS and 10 MHz output from the receiver to communicate frequency corrections from the STL system. An output 1-PPS pin from the oscillator was connected to the oscilloscope for the time interval calculation. A hardware diagram for the second configuration is shown in Figure 4.3.

4.3 On-Board TCXO Results

Two, 24-hour data sets were collected with the first experimental configuration, both of which were started after the receiver solution converged. The time interval measurements from

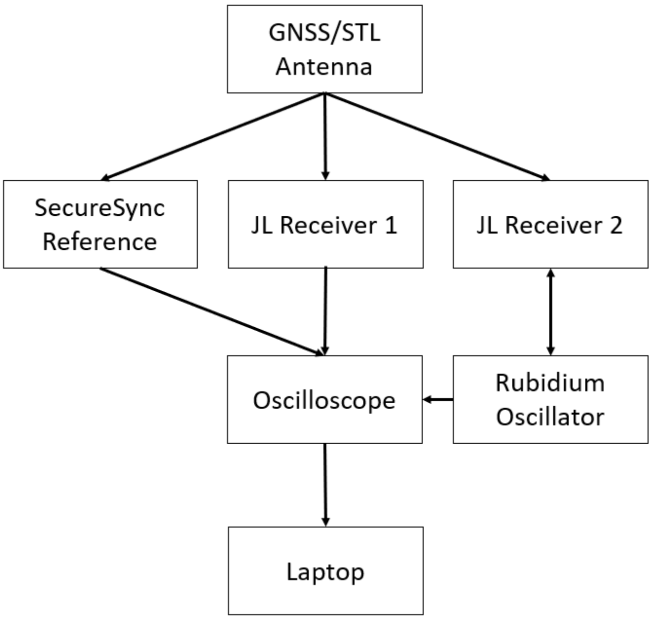

Figure 4.3: Time Interval Hardware Diagram with TCXO and Rubidium Oscillator

the oscilloscope are shown individually in Figure 4.4, and collectively in Figure 4.5. From both plots, it is clear that the receivers are successfully tracking the STL system, and the internal oscillators are being corrected. Additionally, the receiver maintains accuracy to within 300 nanoseconds throughout the duration of the collection period. Since the receiver oscillator is being steered by the navigation solution, this oscillatory behavior in timing is to be expected. The results are summarized through statistical analysis of the time delay measurements in Table 4.1.

Table 4.1: Time Interval Results with Internal TCXO 1

	JL STL-2600 Receiver 1	**JL STL-2600 Receiver 2**
Mean	55.19 ns	43.14 ns
Standard Deviation	84.71 ns	95.96 ns
Magnitude Standard Deviation	55.95 ns	59.59 ns
Maximum Error	286.05 ns	304.41 ns

From the statistical analysis, both receivers performed similarly, which is to be expected. It should be noted that *Magnitude Standard Deviation* differs from the *Standard Deviation* field in that it is calculated from the magnitude of the time delay, as opposed to the signed delay.

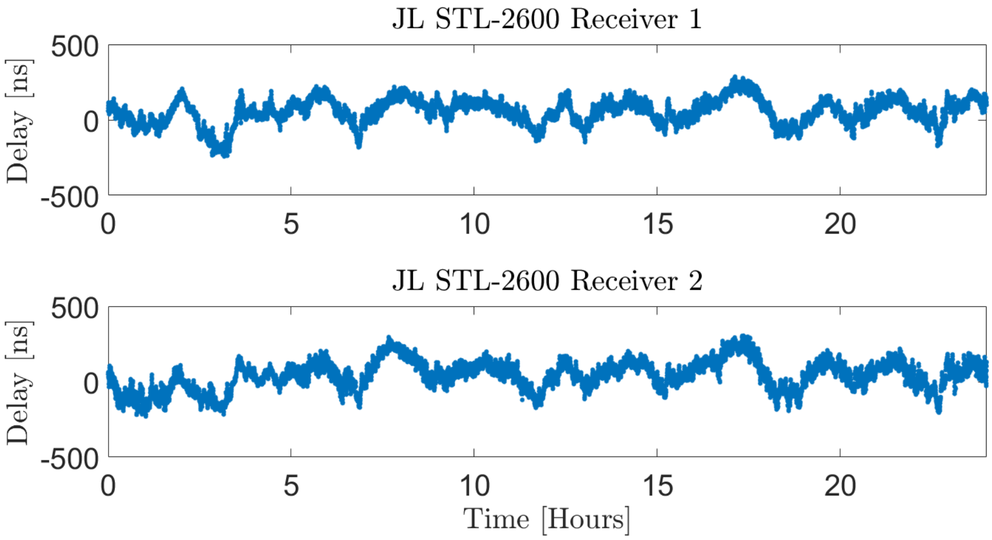

Figure 4.4: Time Interval Individual Results with Internal TCXO 1

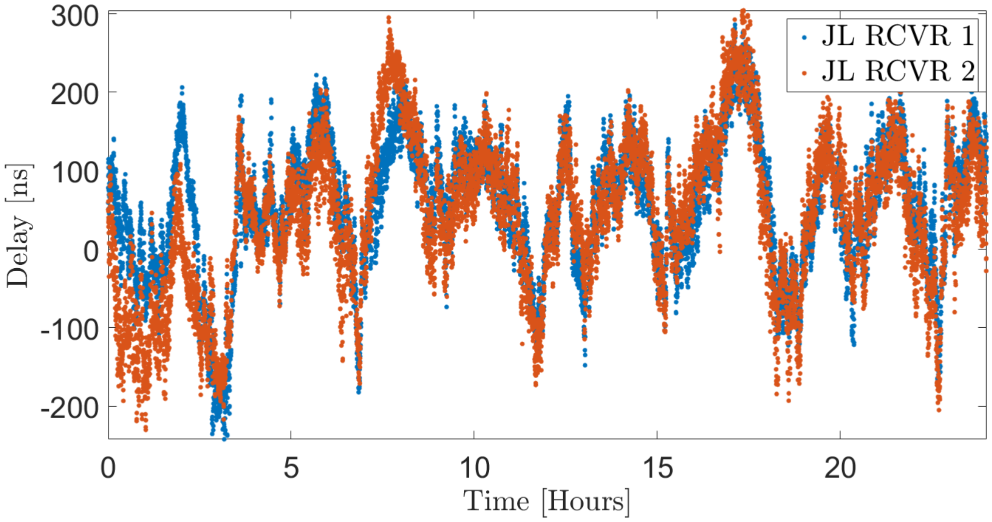

Figure 4.5: Time Interval Collective Results with Internal TCXO 1

This metric provides insight into the variance of the solution about the inherent oscillations. It should also be noted that calibration techniques, such as those presented in [34], could be employed to reduce the mean error for both receivers. The individual and collective results of the second data set collected with Configuration 1 are shown in Figure 4.6 and Figure 4.7, respectively, and the error statistics are presented in Table 4.2.

Again, the two receivers performed similarly. However, as a whole, the data set is noisier than the first. There are several factors which could contribute to the greater errors, including

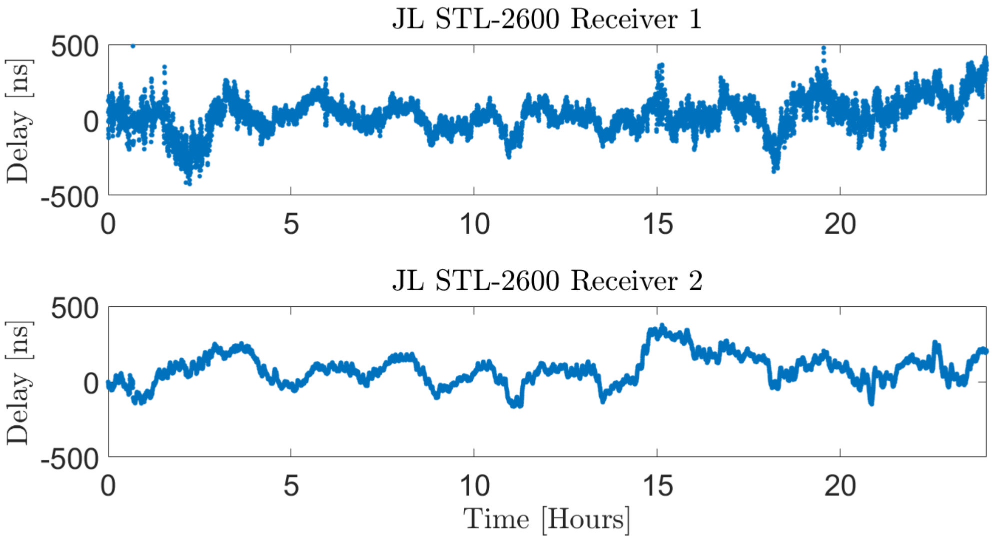

Figure 4.6: Time Interval Individual Results with Internal TCXO 2

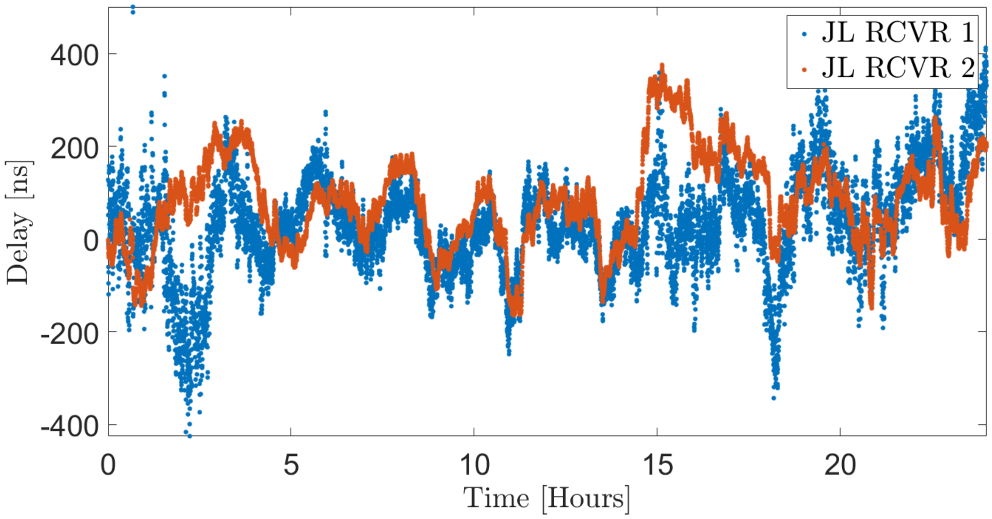

Figure 4.7: Time Interval Collective Results with Internal TCXO 2

Table 4.2: Time Interval Results with Internal TCXO 2

	JL STL-2600 Receiver 1	**JL STL-2600 Receiver 2**
Mean	32.57 ns	82.87 ns
Standard Deviation	109.70 ns	99.60 ns
Magnitude Standard Deviation	73.64 ns	78.24 ns
Maximum Error	500.73 ns	375.61 ns

weather, ionospheric activity, and the STL network outside of the user segment, but no single cause has been identified. Regardless, both receivers maintain nanosecond-level accuracy throughout the duration of the test period. In Figure 4.6, the timing output from Receiver 1 appears to be noisier than the second, which is validated by the standard deviation. However, Receiver 2 produced a smoother timing solution, but demonstrated a greater bias.

4.4 External Rubidium Oscillator Results

The same experiment was conducted with the setup illustrated in Figure 4.3. Again, a 24-hour data set was collected, with measurements being logged every 10 seconds. In this scenario, an external, atomic, rubidium oscillator was integrated into one of the receivers for comparison. Figure 4.8 shows the individual timing results, Figure 4.9 shows the collective results, and Table 4.3 presents the error statistics for both receivers.

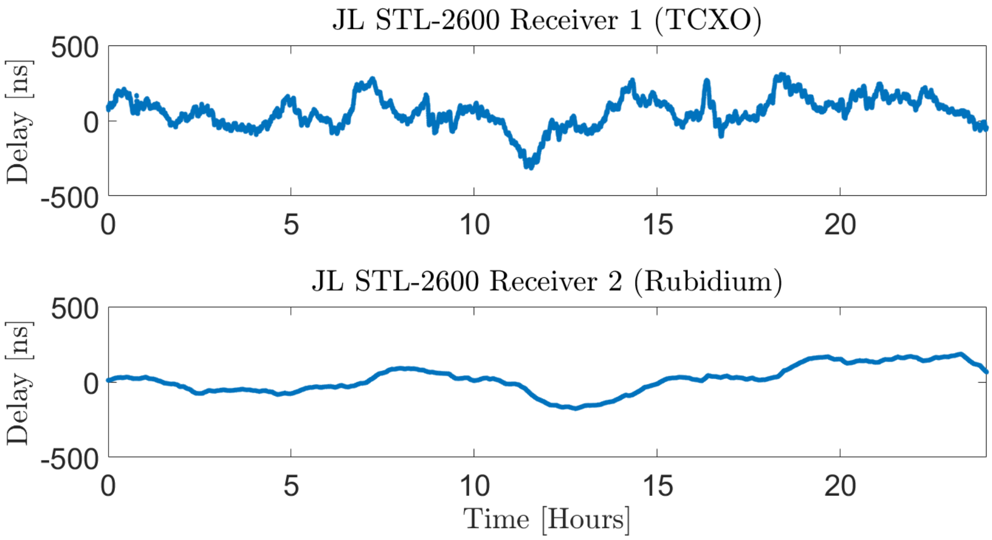

Figure 4.8: Time Interval Individual Results with TCXO and Rubidium Oscillator

Table 4.3: Time Interval Results with TCXO and Rubidium Oscillator

	JL STL-2600 Receiver 1	**JL STL-2600 Receiver 2**
Mean	56.65 ns	17.02 ns
Standard Deviation	102.45 ns	91.44 ns
Magnitude Standard Deviation	72.14 ns	54.84 ns
Maximum Error	315.77 ns	185.90 ns

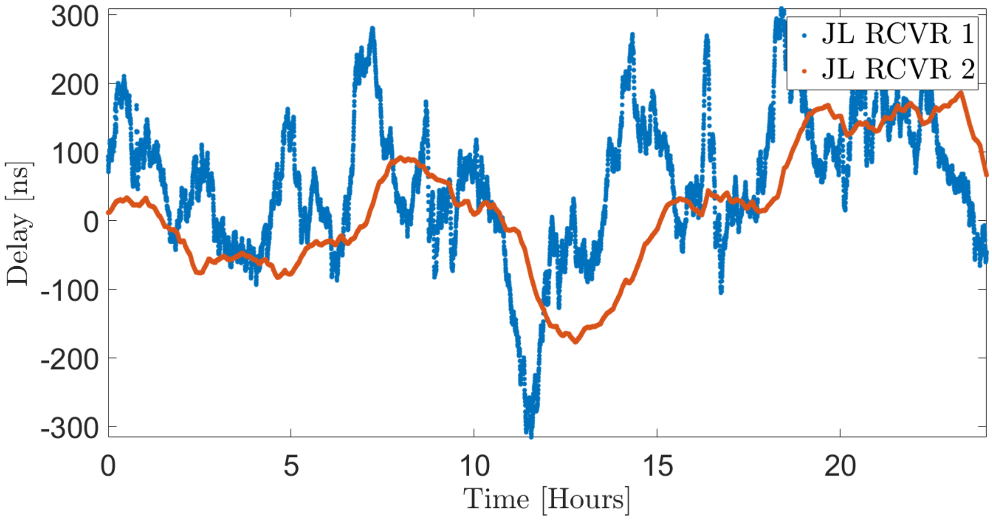

Figure 4.9: Time Interval Collective Results with TCXO and Rubidium Oscillator

From each of the plots, it is clear that the receiver with the integrated atomic oscillator produces a significantly smoother timing solution. Additionally, the oscillation from the use of the rubidium-disciplined receiver has a lower amplitude, which is apparent in the *Standard Deviation* field of the error statistics. Finally, Receiver 2 performs better in every category of the statistical analysis, most obviously in mean and maximum error. Again, in practice, calibration techniques could be used to reduce the mean error.

4.5 Conclusions

In this chapter, a total of 72 hours of data from the Jackson Labs STL-2600 receiver was collected and compared. With the on-board TCXO, the receiver maintained timing accuracy within approximately 500 nanoseconds throughout the entire duration, and performed with less than 110 nanoseconds of standard deviation and 80 nanoseconds of magnitude standard deviation. When the rubidium oscillator was successfully integrated into the receiver hardware, and the timing performance was improved. Specifically, the mean error was reduced by approximately 40 nanoseconds, and the maximum error was reduced by approximately 130 nanoseconds. Additionally, 1-PPS output signal was significantly smoothed, with reduced oscillations and noise. This study demonstrates the capability of the STL system and JL STL-2600 receiver to maintain stable, sub-microsecond level timing accuracy independent of GNSS with either the TCXO or rubidium oscillator.

Chapter 5

Conclusions and Future Work

5.1 Summary

In this thesis, two experiments were conducted to assess the timing capabilities of the STL system using the Jackson Labs STL-2600 receiver. First, raw observables from the receiver were extracted and processed to estimate the receiver clock bias and drift with an EKF and WLS solution. Second, the 1-PPS timing outputs from the receiver module were collected and compared to a GNSS-disciplined reference.

Chapter 1 began with a brief introduction to the motivation for this work and emphasized the usage of satellite-based timing in a variety of industrial and personal systems. A literature review of the prior art in the field of LEO navigation and timing with the STL signal was conducted and summarized, and the contributions of this work to the field were clearly outlined. The chapter concluded with a concise summary of this thesis.

Chapter 2 provided insight into satellite-based navigation. First, a brief history of GPS was discussed. Next, basic navigation principles were presented, including coordinate frames, measurements, and estimation techniques. Then, background of the GPS signal and its limitations were discussed, and the concept of observability was considered. The chapter shifted focus to the Iridium constellation and its potential for timing applications. The Iridium network, various signals, and the STL data message were presented, and the benefits and drawbacks when compared to GPS were emphasized.

Chapter 3 introduced the first experiment conducted in this research, in which raw observables were processed to study the accuracy and convergence of timing solutions. First, an introduction to the study was presented, and the correlation between navigation states and timing was derived. Next, the chapter discussed the hardware components used for this work, including the Jackson Labs STL-2600 receiver module, receiver oscillators, the SecureSync Time and Frequency Reference System, and data collection hardware. Furthermore, the hardware configurations for the first experiment were defined. The chapter identified the estimation algorithms used for this work and derived the application-specific measurement models used. The results from two hardware configurations processed under two scenarios were presented and compared, and conclusions are drawn regarding the effect of a known user position, errors in user position, and receiver clock input.

Chapter 4 continued to the second and final experiment conducted for this thesis. In this study, the estimation process was left to the JL STL-2600 receiver, and only the 1-PPS output voltage signal was considered. The off-the-shelf hardware was used for two collection periods, and similarities and differences of the results were considered. Next, an external, rubidium oscillator was integrated into one of the receivers, and the performance was noticeably improved. The chapter concluded with an overview of the results of the experiment and takeaways from the findings.

Finally, this chapter serves as a concise summary of the thesis in its entirety. Next, broad conclusions regarding the results of both studies are described. Finally, suggestions for avenues of future work are discussed.

5.2 Conclusions

Throughout this study, a total of 5 non-consecutive days of data was collected and processed, of which 48 hours of raw observables were processed, and 72 hours of 1-PPS time intervals were measured. Each study was intended to provide insight into different characteristics of the STL system's performance and gauge expected performance. The overall objective of the study was to investigate the usage of the Iridium STL system as a backup or complement to the existing GPS and GNSS networks. It should be noted that the findings of this study can be interpreted multiple ways. If an total replacement or alternative to GPS is desired, the sample size of data presented in this thesis is relatively small. However, if STL is considered as a holdover or aid to GPS timing, this study makes a convincing case for its efficacy.

In the timing state estimation portion, STL demonstrated sub-microsecond-level timestamping capabilities in both configurations. The findings of both configurations indicated substantial improvement when the receiver position was known. Additionally, the receiver drift was significantly reduced when the external, rubidium oscillator was integrated into the receiver hardware. For both the TCXO and rubidium oscillator, the solution successfully bounded the timing errors to less than 300 nanoseconds. In the sensitivity analysis of receiver position errors, the TCXO-driven configuration showed significant timing variability, particularly in the 500 and 1000 kilometer error tests. However, the rubidium-disciplined implementation was able to minimize the timing errors and maintain stable, accurate time.

In the receiver time interval experiment, the direct 1-PPS outputs of two JL STL-2600 modules were measured against a highly-accurate GNSS timing reference system. In the first configuration, both receivers performed similarly, demonstrating within approximately 500 nanoseconds of error at all times with less than 110 nanosecond standard deviation. When compared to the TCXO configuration collected during the same period, the rubidium oscillator reduced the error mean, standard deviation, and maximum by 47, 11, and 130 nanoseconds, respectively.

In conclusion, the STL network demonstrated nanosecond-level timing accuracy throughout the entirety of this work. Application-specific timing estimation algorithms were implemented, tested, and compared for static receiver conditions. In such, the accuracy, stability, uncertainty, and convergence rates were assessed for each configuration. Finally, the 1-PPS timing capabilities of the newly-released, commercially-available Jackson Labs Technologies STL-2600 receiver module were assessed. Each of these experiments were tested with the off-the-shelf receiver component and with a high-fidelity, external, rubidium oscillator in the loop.

5.3 Future Work

Moving forward, additional analysis and testing is necessary to further validate the STL network as a timing backup or complement to GNSS. The contents of this study were derived from the prior art and contributed further experimental configurations and test scenarios. Potential avenues for advancement in the field of STL timing are as follows.

- The timing capabilities of a dynamic STL receiver have yet to be well-assessed. Observability is the primary challenge in this field, but could potentially be aided with an external sensor.
- Calibration techniques and robust initialization methods could be employed to reduce the mean error in the time interval solution.
- One of the primary advantages to STL timing is the signal strength, the system should be further tested and compared in GNSS-degraded environments, including indoors and dense, urban areas.
- Similar to other areas of research, sample size is critical to verify a system's efficacy. While this work presents results from multiple days of data collection, further testing of the timing state estimation and receiver 1-PPS time interval is required to verify the STL system's efficacy.
- Considering the prominence of GNSS-based timing, a study of GNSS/STL fused navigation solutions could leverage additional measurements to improve timing performance, when compared to each system individually.

References

[1] Thuy Mai. Global Positioning System History, May 2015. Publisher: Brian Dunbar.

[2] CISA. Global Positioning System (GPS) Interference. Technical report, Cybersecurity & Infrastructure Security Agency, December 2022.

[3] Youjing Cui and Shuzhi Sam Ge. Autonomous Vehicle Positioning with GPS in Urban Canyon Environments. *IEEE Transactions on Robotics and Automation*, 19(1):15–25, February 2003.

[4] G. Dedes and A.G. Dempster. Indoor GPS Positioning - Challenges and Opportunities. In *VTC-2005-Fall. 2005 IEEE 62nd Vehicular Technology Conference, 2005.*, volume 1, pages 412–415, Dallas, TX, USA, 2005. IEEE.

[5] Alan Grant, Paul Williams, Nick Ward, and Sally Basker. GPS Jamming and the Impact on Maritime Navigation. *Journal of Navigation*, 62(2):173–187, April 2009.

[6] Alan C O'Connor, Michael P Gallaher, Kyle Clark-Sutton, Daniel Lapidus, Zack T Oliver, Troy J Scott, Dallas W Wood, Manuel A Gonzalez, Elizabeth G Brown, and Joshua Fletcher. Economic Benefits of the Global Positioning System (GPS). Technical Report 0215471, RTI International, June 2019.

[7] Christina Pinell. Receiver Architectures for Positioning with Low Earth Orbit Satellite Signals. Master's thesis, Aalto University, November 2021.

[8] Per Enge, Bart Ferrell, Jeff Bennett, David Whelan, Greg Gutt, and David Lawrence. Orbital Diversity for Satellite Navigation. In *Proceedings of the 25th International Technical*

Meeting of the Satellite Division of The Institute of Navigation (ION GNSS 2012), pages 3834–3846, Nashville, Tennessee, September 2012.

[9] Gabriele Oligeri, Savio Sciancalepore, and Roberto Di Pietro. GNSS spoofing detection via opportunistic IRIDIUM signals. In *Proceedings of the 13th ACM Conference on Security and Privacy in Wireless and Mobile Networks*, pages 42–52, Linz Austria, July 2020. ACM.

[10] Peter H. Dana. Global Positioning System (GPS) Time Dissemination for Real-Time Applications. *Real-Time Systems*, 12(1):9–40, January 1997.

[11] National Coordination Office for Space-Based Positioning, Navigation, and Timing. GPS Accuracy, March 2022.

[12] David C. Mazur, Ryan D. Quint, and Virgilio A. Centeno. Time synchronization of automation controllers for power applications. In *2012 IEEE Industry Applications Society Annual Meeting*, pages 1–8, Las Vegas, NV, USA, October 2012. IEEE.

[13] National Coordination Office for Space-Based Positioning, Navigation, and Timing. Timing, April 2022.

[14] W Lewandowski and E F Arias. GNSS times and UTC. *Metrologia*, 48(4):S219–S224, August 2011.

[15] Ki Young Koo, David Hester, and Sehoon Kim. Time Synchronization for Wireless Sensors Using Low-Cost GPS Module and Arduino. *Frontiers in Built Environment*, 4:82, January 2019.

[16] Ladislav Stastny, Lesek Franek, Miroslav Jirgl, Stefan Misik, and Zdenek Bradac. Time Synchronization in Power-line Communication. *IFAC-PapersOnLine*, 48(4):83–88, 2015.

[17] L. Sliwczynski, P. Krehlik, H. Imlau, H. Ender, H. Schnatz, D. Piester, and A. Bauch. Towards sub-nanosecond synchronization of a telecom network by fiber optic distribution of UTC(k). In *2016 European Frequency and Time Forum (EFTF)*, pages 1–4, York, April 2016. IEEE.

[18] Rohan Kapoor, Subramanian Ramasamy, Alessandro Gardi, and Roberto Sabatini. UAV Navigation using Signals of Opportunity in Urban Environments: A Review. *Energy Procedia*, 110:377–383, March 2017.

[19] Mahdi Maaref, Joe Khalife, and Zak M. Kassas. Integrity Monitoring of LTE Signals of Opportunity-Based Navigation for Autonomous Ground Vehicles. In *31st International Technical Meeting of The Satellite Division of the Institute of Navigation (ION GNSS+ 2018)*, pages 2456–2466, Miami, Florida, October 2018.

[20] Samuel Morgan and Scott Martin. Performance Analysis of a Cellular LTE and GPS L1 C/A Vector Tracking Receiver, a Simulation Study. pages 692–707, Long Beach, California, February 2023.

[21] Kenneth A Fisher. *The Navigation Potential of Signals of Opportunity-based Time Difference of Arrival Measurements*. Ph. D. Dissertation, Air Force Institute of Technology, March 2005.

[22] Joshua J. Morales, Joe Khalife, Ali A. Abdallah, Christian T. Ardito, and Zak M. Kassas. Inertial Navigation System Aiding with Orbcomm LEO Satellite Doppler Measurements. In *31st International Technical Meeting of The Satellite Division of the Institute of Navigation (ION GNSS+ 2018)*, pages 2718–2725, Miami, Florida, October 2018.

[23] Samer Hayek, Joe Saroufim, Mohammad Neinavaie, Sharbel Kozhaya, and Zaher M. Kassas. Assessment of Differential Doppler Navigation with Starlink LEO Satellite Signals of Opportunity. In *2023 International Technical Meeting of The Institute of Navigation*, pages 1021–1031, Long Beach, California, February 2023.

[24] Joe J. Khalife and Zaher M. Kassas. Receiver Design for Doppler Positioning with Leo Satellites. In *ICASSP 2019 - 2019 IEEE International Conference on Acoustics, Speech and Signal Processing (ICASSP)*, pages 5506–5510, Brighton, United Kingdom, May 2019. IEEE.

[25] Hamza Benzerrouk, Quang Nguyen, Fang Xiaoxing, Abdessamad Amrhar, Alexander V. Nebylov, and Rene Landry. Alternative PNT based on Iridium Next LEO Satellites Doppler/INS Integrated Navigation System. In *2019 26th Saint Petersburg International Conference on Integrated Navigation Systems (ICINS)*, pages 1–10, Saint Petersburg, Russia, May 2019. IEEE.

[26] Zizhong Tan, Honglei Qin, Li Cong, and Chao Zhao. Positioning Using IRIDIUM Satellite Signals of Opportunity in Weak Signal Environment. *Electronics*, 9(1):37, December 2019.

[27] M Kassas, Joshua J Morales, and Joe J Khalife. New-Age Satellite-Based Navigation STAN: Simultaneous Tracking and Navigation with LEO Satellite Signals. *Inside GNSS*, 4600, 2019.

[28] Trier R. Mortlock and Zaher M. Kassas. Performance Analysis of Simultaneous Tracking and Navigation with LEO Satellites. In *33rd International Technical Meeting of the Satellite Division of The Institute of Navigation (ION GNSS+ 2020)*, pages 2416–2429, October 2020.

[29] Chao Zhao, Honglei Qin, Ning Wu, and Danyao Wang. Analysis of Baseline Impact on Differential Doppler Positioning and Performance Improvement Method for LEO Opportunistic Navigation. *IEEE Transactions on Instrumentation and Measurement*, 72:1–10, 2023.

[30] Sterling Thompson, Scott Martin, and David Bevly. Single Differenced Doppler Positioning with Low Earth Orbit Signals of Opportunity and Angle of Arrival Estimation. In *2021 International Technical Meeting of The Institute of Navigation*, pages 497–509, Online, February 2021.

[31] David Lawrence, H. Stewart Cobb, Gregory Gutt, Francois Tremblay, Pascal Laplante, and Michael O'Connor. Test Results from a LEO-Satellite-Based Assured Time and Location Solution. In *2016 International Technical Meeting of The Institute of Navigation*, pages 125–129, Monterey, California, February 2016.

[32] Greg Gutt, David Lawrence, Stewart Cobb, and Michael O'Connor. Recent PNT Improvements and Test Results Based on Low Earth Orbit Satellites. *ION Precise Time and Time Interval Meeting*, January 2018.

[33] Andrew Hansen, Stephen Mackey, Hadi Wassaf, Vaibhav Shah, Eric Wallischeck, Christopher Scarpone, Michael Barzach, and Elliott Baskerville. Complementary PNT and GPS Backup Technologies Demonstration Report. Technical report, Department of Transportation, January 2021.

[34] Peter B. Johnson, Andrew N. Novick, and Michael A. Lombardi. Measuring the Timing Accuracy of Satellite Time and Location (STL) Receivers. In *54th Annual Precise Time and Time Interval Systems and Applications Meeting*, pages 207–215, Long Beach, California, February 2023.

[35] Austin M. Smith and David M. Bevly. Precision Timing with LEO Satellite Time and Location Signals. In *Proceedings of the 2023 Precise Time and Time Interval Systems and Applications Meeting*, pages 197–206, Long Beach, California, February 2023. Institute of Navigation.

[36] Norman Bonnor. A Brief History of Global Navigation Satellite Systems. *Journal of Navigation*, 65(1):1–14, January 2012.

[37] NASA. Sputnik 1, October 2022.

[38] Pratap Misra and Per Enge. *Global Positioning System: Signals, Measurements, and Performance*. Ganga-Jamuna Press, Lincoln, Massachusetts, revised second edition, 2012.

[39] U.S. Space Force. Space Segment, June 2022.

[40] Don H. Johnson. Signal-to-Noise Ratio. *Scholarpedia*, 1(12):2088, December 2006.

[41] Paul D. Groves. GPS Signal-to-Noise Measurement in Weak Signal and High-Interference Environments. *Navigation*, 52(2):83–94, June 2005.

[42] R. E. Kalman. A New Approach to Linear Filtering and Prediction Problems. *Journal of Basic Engineering*, 82(1):35–45, March 1960.

[43] Paul D. Groves. *Principles of GNSS, Inertial, and Multisensor Integrated Navigation Systems*. Artech House, 2 edition, 2013.

[44] Jennifer Denise Gautier. *GPS/INS Generalized Evaluation Tool (GIGET) for the Design and Testing of Integrated Navigation Systems*. Ph. D. Dissertation, Stanford University, June 2003.

[45] Christopher Robert Hamm. Analysis of Simulated Performance of Integrated Vector Tracking and Navigation Loops for GPS. Master's thesis, Auburn University, December 2005.

[46] Gianluca Falco, Marco Pini, and Gianluca Marucco. Loose and Tight GNSS/INS Integrations: Comparison of Performance Assessed in Real Urban Scenarios. *Sensors*, 17(2):255, January 2017.

[47] Ch Kreye, B Eissfeller, and G Ameres. Architectures of GNSS/INS Integrations - Theoretical Approach and Practical Tests -. *Symposium on Gyro Technology*, pages 14.0–14.16, 2004.

[48] Matthew Lashley. Kalman Filter Based Tracking Algorithms For Software GPS Receivers. Master's thesis, Auburn University, December 2016.

[49] Matthew Lashley, David M. Bevly, and John Y. Hung. A valid comparison of vector and scalar tracking loops. In *IEEE/ION Position, Location and Navigation Symposium*, pages 464–474, Indian Wells, CA, USA, May 2010. IEEE.

[50] J. J. Spilker Jr. GPS Signal Structure and Performance Characteristics. *NAVIGATION*, 25(2):121–146, 1978. tex.eprint: https://onlinelibrary.wiley.com/doi/pdf/10.1002/j.2161-4296.1978.tb01325.x.

[51] D. Bilitza and B.W. Reinisch. International Reference Ionosphere 2007: Improvements and new parameters. *Advances in Space Research*, 42(4):599–609, August 2008.

[52] W.A. Feess and S.G. Stephens. Evaluation of GPS Ionospheric Time-Delay Model. *IEEE Transactions on Aerospace and Electronic Systems*, AES-23(3):332–338, May 1987.

[53] Lukas Klozar and Jan Prokopec. Propagation path loss models for mobile communication. In *Proceedings of 21st International Conference Radioelektronika 2011*, pages 1–4, Brno, Czech Republic, April 2011. IEEE.

[54] Ozkan Katircioglu, Hasan Isel, Osman Ceylan, Firat Taraktas, and H. Bulent Yagci. Comparing ray tracing, free space path loss and logarithmic distance path loss models in success of indoor localization with RSSI. In *2011 19thTelecommunications Forum (TELFOR) Proceedings of Papers*, pages 313–316, Belgrade, Serbia, November 2011. IEEE.

[55] M. Riback, J. Medbo, J.-E. Berg, F. Harrysson, and H. Asplund. Carrier Frequency Effects on Path Loss. In *2006 IEEE 63rd Vehicular Technology Conference*, volume 6, pages 2717–2721, Melbourne, Australia, 2006. IEEE.

[56] K. Maine, C. Devieux, and P. Swan. Overview of IRIDIUM satellite network. In *Proceedings of WESCON'95*, page 483, San Francisco, CA, USA, 1995. IEEE.

[57] C.E. Fossa, R.A. Raines, G.H. Gunsch, and M.A. Temple. An overview of the IRIDIUM (R) low Earth orbit (LEO) satellite system. In *Proceedings of the IEEE 1998 National Aerospace and Electronics Conference. NAECON 1998. Celebrating 50 Years (Cat. No.98CH36185)*, pages 152–159, Dayton, OH, USA, 1998. IEEE.

[58] Chris Gebhardt. SpaceX: Iridium-5 to launch in March; government shutdown creates manifest uncertainty-NASASpaceFlight.com, January 2018.

[59] Carl E. Fossa, Richard A. Raines, Gregg H. Gunsch, and Michael A. Temple. A Performance Analysis of the IRIDIUM Low Earth Orbit Satellite System with a Degraded Satellite Constellation. *ACM SIGMOBILE Mobile Computing and Communications Review*, 2(4):54–61, October 1998.

[60] Tyler G.R. Reid, Todd Walter, Per K. Enge, David Lawrence, H. Stewart Cobb, Greg Gutt, Michael O'Connor, and David Whelan. Navigation from Low Earth Orbit: Part 1: Concept, Current Capability, and Future Promise. In Y. T. Jade Morton, Frank Diggelen, James J. Spilker, Bradford W. Parkinson, Sherman Lo, and Grace Gao, editors, *Position, Navigation, and Timing Technologies in the 21st Century*, pages 1359–1379. Wiley, 1 edition, December 2020.

[61] Kirk Vespestad. STL-2600: New User Equipment from Jackson Labs Technologies, February 2021.

[62] Inside GNSS. New GNSS-Independent Receiver Generates Nanosecond Timing, Meter-Level Accuracy from Low-Earth Orbit Satellite Signals, February 2021.

[63] D.W. Allan. Statistics of atomic frequency standards. *Proceedings of the IEEE*, 54(2):221–230, 1966.

[64] Ondrej Baran and Miroslav Kasal. Allan variances calculation and simulation. In *2009 19th International Conference Radioelektronika*, pages 187–190, Bratislava, April 2009. IEEE.

[65] D W Allan, David A Howe, F L Walls, and D B Sullivan. Characterization of Clocks and Oscillators. Technical Report NBS TN 1337, National Bureau of Standards, Gaithersburg, MD, 1990. Edition: 0.

[66] IEEE Standards Coordinating Committee 27. IEEE Standard Definitions of Physical Quantities for Fundamental Frequency and Time Metrology—Random Instabilities. Technical report, IEEE, February 2009. ISBN: 9780738168555 9780738168562.

[67] Peter W Sarunic. Development of GPS Receiver Kalman Filter Algorithms for Stationary, Low-Dynamics, and High-Dynamics Applications. *Cyber and Electronic Warfare Division Defence Science and Technology Group*, page 57, June 2016.

[68] Robert Brown and Patrick Hwang. *Introduction to Random Signals and Applied Kalman Filtering*. John Wiley & Sons, Inc., fourth edition, 2012.

[69] SRS. Rubidium Frequency Standard - FS725, December 2015.

[70] Safran Electronics & Defense. SecureSync 2400 Resilient Time and Frequency Synchronization Platform, February 2023.

[71] Antti Lehtinen. Doppler Positioning with GPS. Master's thesis, Tampere University of Technology, March 2002.